PAPER

Numerical investigation of AC arc ignition on cold electrodes in atmospheric-pressure argon

To cite this article: D F N Santos *et al* 2021 *J. Phys. D: Appl. Phys.* **54** 195202

View the article online for updates and enhancements.

Numerical investigation of AC arc ignition on cold electrodes in atmospheric-pressure argon

D F N Santos[1,2] , **M Lisnyak**[3], **N A Almeida**[1,2] , **L G Benilova**[1] **and M S Benilov**[1,2]

[1] Departamento de Física, Faculdade de Ciências Exatas e da Engenharia, Universidade da Madeira, 9000 Funchal, Portugal
[2] Instituto de Plasmas e Fusão Nuclear, Instituto Superior Técnico, Universidade de Lisboa, 1049-001 Lisboa, Portugal
[3] Schneider Electric Science and Technology, 38050 Cedex 9 Grenoble, France

E-mail: benilov@staff.uma.pt

Abstract

Since experiments cannot clarify the mechanism of current transfer to non-thermionic arc cathodes, this can only be done by means of numerical modelling based on first principles and not relying on *a priori* assumptions. In this work, the first quarter-period after the ignition of an AC arc on cold electrodes in atmospheric-pressure argon is investigated by means of unified one-dimensional modelling, where the conservation and transport equations for all plasma species, the electron and heavy-particle energy equations, and the Poisson equation are solved in the whole interelectrode gap up to the electrode surfaces. Results are compared with those for DC discharges and analysed with the aim to clarify the role of different mechanisms of current transfer to non-thermionic arc cathodes. It is found that the glow-to-arc transition in the AC case occurs in a way substantially different from the quasi-stationary glow-to-arc transition. The dominant mechanisms of current transfer to the cathode during the AC arc ignition on cold electrodes are, subsequently, the displacement current, the ion current, and thermionic emission current. No indications of explosive emission are found. Electron emission from the impact of excited atoms can hardly be a dominant mechanism either. The introduction of the so-called field enhancement factor, which is used for description of field electron emission from cold cathodes in a vacuum, leads to computed cathode surface temperature values that are appreciably lower than the melting temperature of tungsten even in the quasi-stationary case. This means that pure tungsten cathodes of atmospheric-pressure argon arcs can operate without melting, in contradiction with experiments.

Keywords: AC arc ignition, AC arc discharges, non-thermionic cathodes, arc discharges

(Some figures may appear in colour only in the online journal)

1. Introduction

The cathodes of high-pressure arc discharges are conventionally divided into hot, or thermionic, and cold, or non-thermionic, cathodes. Thermionic cathodes operating in nonoxidizing plasma-producing gases are usually made of refractory metals, examples being tungsten cathodes used in high-intensity discharge lamps and gas tungsten arc welding, or graphite. Thermionic cathodes operating in plasma-producing gases containing oxygen, including air, are made of metals which, when interacting with plasma, are oxidized and coated with an oxide layer with good thermostable and electron-emission properties, zirconium and hafnium being the metals most commonly used. Non-thermionic cathodes are mostly made of metals with a relatively low boiling point, e.g. water-cooled copper cathodes of arc plasma torches and silver

cathodes of low-voltage circuit breakers. Another important example of non-thermionic cathodes is steelwork pieces under conditions of gas metal arc welding, which operate as cathodes of the arc discharge.

There is a large number of papers devoted to various aspects of the theory and modelling of thermionic cathodes, many of them published recently, e.g. reviews [1, 2]. In particular, it is well established that while the thermionic electron emission mechanism contributes most of the electric current to the surface of a thermionic cathode, the contribution of the ions coming from the plasma is minor but non-negligible, usually in the order of one to a few tenths. The cathode surface is heated by energy fluxes carried by heavy particles and fast plasma electrons, and is cooled by thermionic emission. The temperature of the thermionic cathode surface and the electric current density inside the arc cathode attachment are in the range 3000–4000 K and 10^6–10^8 A m^{-2} respectively, depending on conditions.

In contrast, the understanding of the operation of non-thermionic cathodes remains poor. It is frequently assumed that the dominating mechanism of current transfer to the surface of a non-thermionic cathode is thermo-field electron emission (e.g. review [3]); however, alternative mechanisms of electron emission are considered as well, e.g. explosive/evaporative and field emission (e.g. book [4]) or electron emission from the impact of excited atoms (the recent paper [5]). In the LTE (local thermodynamic equilibrium) modelling of high-pressure arc discharges, the heating of non-thermionic cathodes by the electric current is estimated as jV_c, where j is the current density and V_c is the cathode sheath voltage, which accelerates ions [3]; this implies that the dominating mechanism of current transfer to non-thermionic cathodes is the charge transport by ions coming to the cathode surface from the plasma. The current density inside arc attachments to non-thermionic cathodes, if estimated in terms of the measured area of erosion traces, is of the order of 10^8 A m^{-2}; however, it is unknown how much current flows outside the erosion sites, so this value is rather an upper estimate.

Since the experiment cannot clarify the mechanism of current transfer to non-thermionic arc cathodes, this can only be done by a means of numerical modelling that is sufficiently general and does not rely on *a priori* assumptions on physical mechanisms that are dominant in different discharge regions. The most general approach to modelling high-pressure arc plasmas is so-called unified modelling, where a single set of differential equations, comprising conservation and transport equations for all plasma species, the electron and heavy-particle energy equations, and the Poisson equation, is solved in the whole interelectrode gap up to the electrode surfaces. Simulations of atmospheric-pressure argon arc discharges performed by this approach have been described in the literature [6–17]; however, they are highly computationally intense and their application has been limited up to now to two situations: one-dimensional (1D) modelling, which includes modelling of near-electrode layers of high-current arcs [6, 7, 9, 13, 14] and modelling of microdischarges with low current densities [11, 15, 16], and two-dimensional (2D) modelling of low-current arcs [8, 10, 12, 17]. The case of thermionic cathodes is

considered in all of these works except for the papers [8, 12] dedicated to simulation of gliding arcs. The results of unified 1D and 2D modelling of microarcs were compared with each other in [17], with the conclusion that the 1D model allows the study of properties of microarcs with high spatial resolution at low computational costs and is capable of predicting plasma properties in good agreement (typically within approximately 5%) with the 2D model.

A defining feature of the unified modelling approach is that it does not require division of the plasma computation domain into regions governed by different physical mechanisms, such as LTE bulk plasma and non-equilibrium near-electrode layers. Therefore, there is no need to *a priori* theorize about governing mechanisms; rather, regions governed by different physical mechanisms will appear in due course in the results of the modelling, a very important advantage of the unified approach. At the same time, this feature represents a limitation: arc discharges do contain regions governed by different physical mechanisms, which, strictly speaking, should not be described by a single system of equations. For example, collisionless near-cathode space-charge sheaths with two groups of electrons (those emitted by the cathode surface and electrons coming from the bulk plasma), strictly speaking, cannot be described by the same equations as the collision-dominated quasi-neutral plasma. Moreover, not all kinetic and transport processes in arc plasmas are well studied, which inevitably introduces uncertainties into any numerical modelling.

Fortunately, the extensive experience in modelling of arc plasma interaction with thermionic cathodes reported in the literature has shown that integral characteristics predicted by different theoretical models are not strongly affected by details of descriptions of plasma processes (such as the ion motion in the sheath being collision-free or collision-dominated or the distribution of the heavy-particle energy flux from the plasma to the cathode surface between the atoms and the ions), provided that the basic physics accounted for in the model is right; e.g. [2, 18] and references therein. Accordingly, results given by different models are close to each other in many aspects. This gives a reasonable degree of confidence in the modelling results, especially as far as qualitative conclusions are concerned.

In this work, unified 1D modelling of the ignition of an AC arc on cold electrodes in atmospheric-pressure argon is performed. This approach allows one to describe, in a natural way, the whole process of arc development including the switching of polarity; however, the results reported in this work refer to the first quarter-period. Results are compared with those for DC discharges and analysed with the aim to clarify the role of different mechanisms of current transfer to non-thermionic arc cathodes.

The outline of the paper is as follows. The numerical model is described in section 2. Two potential mechanisms of current transfer to cold cathodes are studied in sections 3 and 4: ion current and electron emission from impact of excited atoms. Ignition of arcs on cold cathodes is studied in section 5 taking account of the coupling between processes in the plasma and the heat propagation inside the electrodes. The effect of field to thermo-field emission with electric field enhancement

J. Phys. D: Appl. Phys. **54** (2021) 195202

D F N Santos *et al*

at the cathode surface is studied in section 6. A summary and concluding remarks are given in section 7.

2. Numerical model

2.1. System of equations

The system of equations is the same as the one used in [6, 7, 9, 13, 14] except that the species conservation equations and the heavy-particle and electron energy equations are written in non-stationary form. Analysis shows, somewhat surprisingly, that there is no universal agreement in the literature on the proper form of non-stationary term in the electron energy equation. For completeness, a concise derivation is given in appendix A; the non-stationary term in the derived electron energy equation is the same as that in the book [19] but differs from that in another classic book [20] and in the Plasma module of COMSOL Multiphysics® [21].

The ignition of a discharge in a cold atmospheric-pressure atomic gas between two parallel cold electrodes with a subsequent transition to an arc is considered. Since the most important phenomena governing this transition occur in the immediate vicinity of the cathode, the convective transport of particles and energy is neglected and the hydrodynamic equations are not included. The plasma is comprised by neutral particles (atoms), singly charged ions, and electrons. The effect of the excited atoms is taken into account in terms of stepwise ionization/recombination; this approach predicts plasma parameters with differences of the order of several percent compared to more complex models, which take into account excited atomic states as separate species [22]. The presence of multiply charged ions is neglected as justified in [23]. Also neglected are effects related to the eventual presence of molecular ions and dimers, which are expected not to play a major role in the underlying physics; cf [17]. The heavy-particle species (the atoms and the ions) have temperature T_h and the electron distribution function is Maxwellian with the temperature T_e.

The species conservation equations and the heavy-particle and electron energy equations are equations (13), (17), and (19) of appendix A, respectively, written in one dimension in space and with the material derivatives d/dt being replaced with the local derivatives $\partial/\partial t$. The index α takes values i, a, and e, referring to ions, atoms, and electrons, respectively, in equation (13), and values i and a in the sums on the right-hand side (rhs) of equations (17) and (19). The third term on the rhs of equation (17), accounting for the work of the viscous stress, is dropped. Note that, except for terms with time derivatives, the above equations coincide with the corresponding equations employed in [6], which are equations (1), (10), and (11) of [6]. Moreover, the set of plasma equations includes the multicomponent diffusion equations, written in the form of Stefan–Maxwell equations, equation (5) of [6] with $\mathbf{v}_\alpha$ and $\mathbf{v}_\beta$ replaced by $\mathbf{V}_\alpha$ and $\mathbf{V}_\beta$, and the Poisson equation (the Gauss law), equation (17) of [6]. A transformation of the species conservation and Stefan–Maxwell equations, required before they can be solved numerically, is described in appendix B.

The assumption of negligible convection requires that the force exerted by the electric field over the plasma be compensated by the plasma pressure gradient. It follows that

$$p - \varepsilon_0 \frac{E^2}{2} = p_0, \tag{1}$$

where $p = (n_i + n_a)kT_h + n_e kT_e$ is the plasma pressure, E is the x-projection of the electric field vector, and p_0 is a known parameter, which may be interpreted as the plasma pressure in the arc chamber.

Results reported in this work refer to argon plasma under atmospheric pressure, $p_0 = 1$ bar. The transport, kinetic, and radiation coefficients of the argon plasma are evaluated using formulas [6].

Trial simulations have shown that the second term on the rhs of equation (17), accounting for the work of the pressure force, while being normally insignificant, is unphysically large in certain cases. The latter is a consequence of the fact that variations in the electron pressure, which may be very fast, by virtue of equation (1) are instantly reflected in the heavy-particle pressure and, therefore, in the plasma density. In other words, this is a consequence of limitations stemming from the assumption of negligible convection. Fortunately, this is not a major problem, since the term in question has practically no effect on the solution in most cases and does not produce qualitative changes even in cases where it is unphysically large. We note for definiteness that the modelling reported in this work was performed with the second term on the rhs of equation (17) being dropped.

The set of governing equations also includes the heat conduction equations inside the electrodes, written in the non-stationary 1D form

$$\rho_s C_{ps} \frac{\partial T_s}{\partial t} = \frac{\partial}{\partial x} \left(\kappa_s \frac{\partial T_s}{\partial x} \right), \tag{2}$$

where T_s is the electrode temperature and ρ_s, C_{ps}, and κ_s are the mass density, the specific isobaric heat capacity, and the thermal conductivity of the electrode material. Note that the latent heat of melting is included in C_{ps}.

2.2. Boundary conditions

The system of plasma equations is solved in the domain $0 \leqslant x \leqslant h$, where h is a known parameter (the discharge gap). The heat conduction equations (2) are solved in the inside of the electrodes, which are domains $-h_1 < x < 0$ and $h < x < h + h_2$, where h_1 and h_2 are known parameters (electrode thicknesses).

The boundary conditions for the plasma equations at the electrode surfaces $x = 0$ and $x = h$ are similar to those in [6, 7]. Let us restrict the consideration with the case where all the ions coming from the plasma recombine at the electrode surface (and the neutral atoms go back into the plasma) and all the electrons coming from the plasma are absorbed by the surface. The boundary condition for the electron density at the electrode surfaces is written as

$$J_e = n \left(\frac{j_{em}}{e} - \frac{n_e C_e}{4} \right), \tag{3}$$

where $C_e = (8kT_e/\pi m_e)^{1/2}$ is the mean speed of random motion of the electrons evaluated in terms of the local electron temperature, $n = 1$ for $x = 0$ and $n = -1$ for $x = h$, and J_e and J_i here and further are projections along the *x*-axis of the vectors of density of transport flux of the electrons and the ions, respectively. Note that equation (3) is equivalent to the so-called Thomson–Loeb formula, which has been widely used in fluid modelling of gas discharges; e.g. [24] and references therein. The density j_{em} of the electron emission current is evaluated as

$$j_{em} = j_{TF} + j_{se}, \tag{4}$$

where j_{TF} is the density of the electron emission current caused by high values of the cathode surface temperature and/or electric field directed to the cathode surface and j_{se} is the density of the secondary electron emission current. The evaluation of both quantities depends on the direction of the local electric field. (Note that one would expect intuitively that the electric field at both electrode surfaces is directed from anode to cathode; however, this does not happen in all cases.) If $nE < 0$, meaning that the local electric field is directed from the plasma to the electrode surface, then j_{TF} is determined taking into account field to thermo-field to thermionic electron emission mechanisms and j_{se} is evaluated as $j_{se} = -e\gamma n J_i$. Here, γ is the so-called effective secondary emission coefficient, which is assumed to characterize all mechanisms of secondary electron emission (due to ion, photon, and excited species bombardment; e.g. section 4.7.2 of [25]). If $nE > 0$, then j_{TF} is evaluated taking into account only the thermionic emission mechanism, i.e. by means of the Richardson formula without the Schottky correction, and j_{se} is set equal to zero. The work function A_f of the electrode material is set equal to 4.5 eV, which is a value characteristic of many metals [26], including tungsten and copper. Note that this or similar values have been used in many modelling studies of thermionic cathodes where a reasonably good agreement has been found with experiments; e.g. [18].

The electron emission current density j_{TF} in the case $nE < 0$ was determined, taking account of field to thermo-field to thermionic mechanisms, in one of two ways. The first way was to use public code [27], which evaluates the Murphy–Good formalism [28]. The code is based on the numerical method [29], provides a calculation accuracy of 10^{-3} over the entire range of conditions for the applicability of the Murphy–Good theory from field to thermo-field to thermionic emission, and does not require *a priori* determination of a specific electron emission mechanism for the conditions considered. The second way was to use the Richardson–Schottky formula. We note here that the electric field computed at the cathode surface was below 10^8 V m^{-1} in all the calculations presented in this work. The electron emission current density values determined by both methods were very close to each other in this field range; for example, for $|E| = 10^8$ V m^{-1} they differed by less than 1.5% over the entire range of cathode surface temperature values T_c

where j_{TF} exceeds 1 A m^{-2} (which is $T_c \gtrsim 1650$ K). Therefore, it is not surprising that the simulation results presented in this work, with the exception of those given in section 6, do not depend on whether j_{TF} was determined by means of the Murphy–Good formalism or the Richardson–Schottky formula.

The boundary condition for the ion density at the electrode surfaces is

$$J_i = -n \frac{n_i C_i}{2}, \tag{5}$$

where $C_i = (8kT_h/\pi m_i)^{1/2}$. Note that the factor of two in the denominator of the term on the rhs (instead of four, as in the second term in the parentheses on the rhs of equation (3)) corresponds to the ion distribution function being strongly anisotropic in the vicinity of an absorbing surface.

The boundary conditions for the heavy-particle and electron temperatures at the electrode surface are

$$T_h = T_s, \tag{6}$$

$$q_e = n \left(\frac{j_{em}}{e} 2kT_s - \frac{n_e C_e}{4} 2kT_e \right). \tag{7}$$

q_e and q_h here and further are projections along the *x*-axis of the vectors of the density of flux of thermal energy of the electrons and the heavy particles, respectively.

The electrostatic potential φ is set equal to zero at one of the electrodes: $\varphi = 0$ for $x = 0$. The lacking boundary condition for the plasma equations may be obtained by specifying the discharge voltage:

$$x = h : \quad \varphi = V_a, \tag{8}$$

where the discharge voltage $V_a = V_a(t)$ is considered as a known function of time. An alternative to using (8) is to specify the electric current density *j*:

$$e(J_i - J_e) + \varepsilon_0 \frac{\partial E}{\partial t} = j, \tag{9}$$

where $j = j(t)$ is considered as a known function of time.

The treatment in this work is focused on unipolar regimes of current transfer. Let us assume for definiteness that $V_a > 0$, so $x = 0$ is the cathode surface and $x = h$ is the anode surface. Then, $j < 0$ in most cases. (Exceptions are possible for very low V_a, where the current is of diffusive nature.) It is convenient, therefore, to designate $-j = j_c$, where j_c has the meaning of the projection of the current density vector along the direction from anode to cathode (which is opposite to the *x*-axis).

Let us proceed to the boundary conditions for equation (2), describing heat conduction inside the electrodes. The boundary condition at the electrode surface bordering the plasma, $x = 0$ or $x = h$, is the condition of continuity of energy flux, which may be written as

$$-\kappa_s \frac{\partial T_s}{\partial x} = q_h + q_e + A_f J_e + (A_i - A_f) J_i, \tag{10}$$

where A_i is the ionization energy of the plasma-producing gas (15.76 eV for argon). Note that the rhs represents, up to sign, the energy flux coming from the plasma to the electrode surface; cf equation (31) of [6]. The left-hand side (lhs) represents the energy removed by heat conduction from the surface into the body of the electrode.

The temperatures at the bottom of the electrodes are controlled by external cooling, so the lacking boundary condition is

$$x = -h_1 : \ T_s = T_{s1}; \qquad x = h + h_2 : \ T_s = T_{s2}, \qquad (11)$$

where T_{s1} and T_{s2} are given quantities.

3. Ion current to cold electrodes

Charge transport by ions coming to the cathode surface from the plasma is one of the hypothetical mechanisms of current transfer to non-thermionic arc cathodes mentioned in the Introduction. Ion current is of primary importance also in the field and thermo-field electron emission mechanisms; these mechanisms require a very high electric field directed to the cathode surface, and such fields may be induced only by positive space charge formed by ions coming from the plasma. It is of interest in this connection to evaluate the maximum current density that can be transported by ions diffusing to the surface of a cold cathode from the bulk of atmospheric-pressure arcs.

The ion current density in the bulk of the arc plasma is low and the ion current coming to the cathode is formed in the near-cathode region; the ions are generated through ionization of neutral atoms by electron impact and then diffuse to the cathode surface. The energy for generation of the ions comes from the electron gas, and if the supply of energy to the electron gas in the near-cathode region is too low, then the lack of the ionization energy may limit the ion current to the cathode. Another potential limitation stems from a finite rate of ambipolar diffusion of the ions.

A simple estimate of the ion ambipolar diffusion rate may be obtained by means of the analytical formulas cited in appendix C. The maximum ion current density that can be transported by ambipolar diffusion of the ions from atmospheric-pressure argon and air plasmas to a negative surface is shown in figure 12 of appendix C. (j_i is the density of ion current to the cathode surface, which is related to the ion transport flux J_i by the formula $j_i = -e \, J_i|_{x=0}$.) One can see that j_i is of the order of 10^7 A m^{-2}. Note that this value is lower than the supposed current density inside the non-thermionic cathode arc attachments of 10^8 A m^{-2}, as mentioned in Introduction. However, given that the latter is merely an upper estimate, these values do not look inconsistent with the hypothesis of an ion current mechanism of current transfer to non-thermionic cathodes.

The estimate of ambipolar-diffusion ion current shown in figure 12 of appendix C, while being useful, does not take into account the limitation stemming from eventual lack of ionization energy in the near-cathode layer mentioned above. In order to obtain a more general estimate, the plasma equations
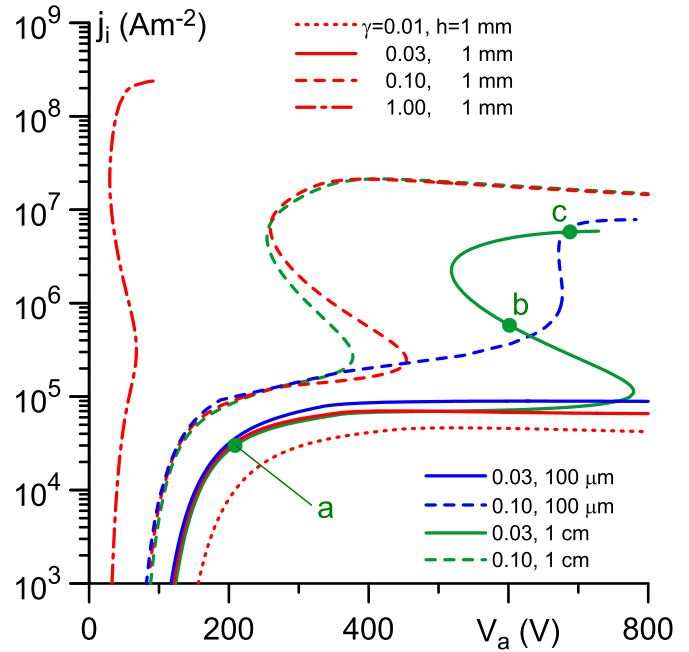

Figure 1. Density of ion current to the cold cathode surface for different values of the secondary electron emission coefficient γ and discharge gap width h. The electrode surface temperatures $T_c = T_a = 1500$ K. The three states marked by the circles are illustrated by figure 2.

described in section 2.1, supplemented with boundary conditions (3)–(9), have been solved for the stationary case for atmospheric-pressure argon plasma with the temperatures of the cathode and anode surfaces, T_c and T_a, equal to 1500 K. (In other words, the electrode heat conduction part of the problem, described by equation (2) and boundary conditions (10) and (11), was discarded and replaced with given electrode surface temperatures of 1500 K.) Note that j_{TF} given by the Murphy–Good formalism is extremely small in these conditions and the only non-zero component of the emission current j_{em} is the secondary electron emission current j_{se}.

The computed ion current density to the cathode surface is shown in figure 1 for several values of the effective secondary electron emission coefficient γ and three values of the interelectrode gap, $h = 100$ μm, 1 mm, and 1 cm. Five of the eight lines shown in figure 1 (the three lines referring to $\gamma = 0.10$ and the ones referring to $\gamma = 1$, $h = 1$ mm and $\gamma = 0.03$, $h = 1$ cm) are S-shaped, and it seems possible that the remaining three lines would also reveal S-shapes if they were calculated over a wider range of conditions. Note that the upper part of the S-shape was not computed up to $V_a = 800$ V in the cases $\gamma = 1$, $h = 1$ mm; $\gamma = 0.1$, $h = 100$ μm; or $\gamma = 0.03$, $h = 1$ cm due to loss of convergence.

It is of interest to compare the characteristic features of states belonging to different sections of the S-shape. As a representative example, distributions of the ion and electron densities for three states marked by circles in figure 1 are shown in figure 2. The states *a*, *b*, and *c* belong to, respectively, the lower, intermediate, and upper sections
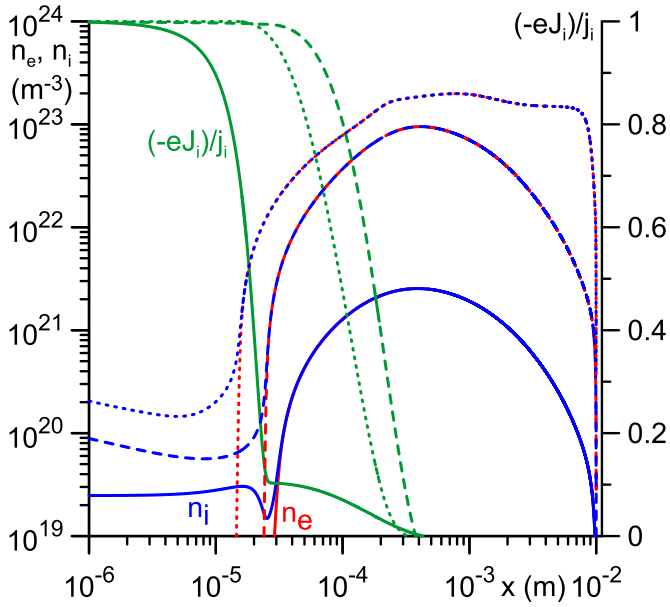
Figure 2. Distributions of the ion and electron densities and the normalized ion current in the direction towards the cathode. $\gamma = 0.03$, $h = 1$ cm, $T_c = T_a = 1500$ K. Solid: state marked a in figure 1. Dashed: state b. Dotted: state c.

of the S-shape. As expected, the bulk plasma is quasi-neutral, $n_i \approx n_e$, in all three states. Deviations from the quasi-neutrality are localized in regions adjacent to the electrodes, or near-electrode space-charge sheaths. (The near-anode space-charge sheath is not visible on this scale.) The thickness of the cathode sheath slowly decreases with increasing current, from approximately 30 μm for $j_c = 3.4 \times 10^4$ A m^{-2} (state a) to approximately 15 μm for $j_c = 5.8 \times 10^6$ A m^{-2} (state c).

Also shown in figure 2 is the density of the ion current in the direction towards the cathode, $(-eJ_i)$, normalized by the value at the cathode surface j_i. There is a noticeable change of inclination of the curve $(-eJ_i)$ for the state a at the edge of the cathode sheath and it is seen that about 90% of the total ion current to the cathode is generated inside the sheath and about 10% is generated in the quasi-neutral plasma adjacent to the sheath. The analysis of the distributions of the ion current density in other states belonging to the lower section of the S-shape, which are not given here for brevity, shows that the contribution of the cathode sheath to the total ion current decreases as the voltage increases and becomes small in the vicinity of the turning point that separates the lower and intermediate sections. All of the ion current is generated in the quasi-neutral plasma in states belonging to the intermediate and upper sections, as exemplified by the distributions of the ion current density in states b and c shown in figure 2.

The analysis of the electron and heavy-particle temperature distributions, which are not given here for brevity, shows that in the state c the temperatures T_e and T_h over the range of distances x from about 2–8 mm differ very little from each

other and vary little in space, from approximately 14.4×10^3–13.3×10^3 K. The electron density varies little as well, which is seen in figure 2, from approximately 1.6×10^{23} to 1.2×10^{23} m^{-3}. One can say that there is a more or less uniform arc column in state c, a feature that distinguishes this state from b and a.

Thus, characteristic features of states belonging to lower or upper sections of the S-shape are, respectively, a significant ion current generated in the near-cathode sheath or the existence of a relatively uniform arc column.

One can see from figure 1 that values of V_a necessary to extract an ion current of the order of 10^5 A m^{-2} or higher are in the order of hundreds of volts, i.e. much higher than the voltage for conventional arc discharges with hot cathodes. Analysis of computation results shows that virtually all of the voltage applies to the near-cathode region. For $\gamma = 0.03$ and V_a in the range between approximately 300 and 500 V, j_i is only weakly dependent on the gap width and the discharge voltage and varies over the range $(0.6$–$0.9) \times 10^5$ A m^{-2}. For $\gamma = 0.1$, j_i may be much higher, of the order of 10^7 A m^{-2}, in agreement with the data shown in figure 12.

In the case of thermionic cathodes, the supply of energy to the electron gas in the near-cathode region and, consequently, of ionization energy is provided by the work of the sheath electric field on electrons emitted by the cathode surface [6]. The same is true for the case of cold cathodes considered here, although the emission mechanism is different: secondary electron emission instead of thermionic emission. This follows from analysis of the energy balance of electron gas in the near-cathode region, which is skipped for brevity and is similar to the analysis given in section 3.2 of [6]; see, in particular, figure 8 of [6]. Note that about two thirds of the energy supplied by the sheath electric field to the emitted electrons is spent on ionization and the rest is transported into the plasma as the electron thermal energy flux, which is dominated by the enthalpy transport by electron current. Thus, the source of the ionization energy in the near-cathode region on cold cathodes is the acceleration of the secondary emitted electrons by the sheath electric field. The strong effect of γ on j_i, seen in figure 1, is consistent with this conclusion and, moreover, indicates that the ion current is limited by the lack of the ionization energy in the near-cathode region, which is caused by the electron emission current being very low.

One can conclude that the current transported by ions diffusing to the surface of a cold cathode from the bulk of an atmospheric-pressure argon arc may reach an order of magnitude of 10^7 A m^{-2} for high values of the discharge gap width and/or secondary electron emission coefficient; however, this would require very high discharge voltages of several hundred volts. The reason the voltages are that high is that the ion current is limited not by a finite ion diffusion rate but rather by the lack of ionization energy in the near-cathode region, and the latter stems from low values of the electron emission current from cold cathodes (secondary emission only). Note that this conclusion is relevant also to the analysis of spotless vacuum arc attachments to hot cathodes; cf review [30] and references therein.

6

4. Electron emission from impact of excited atoms

It is proposed in the recent paper [5] that the most significant electron emission process at the cathodes made of non-thermionic materials is the secondary electron emission under the impact of excited states of atoms of the arc gas, produced in the near-cathode region.

It is assumed in [5] that the excited atoms have secondary emission coefficients of order unity, similar to those observed for metastable atoms, while the effective coefficient of ion-electron emission is 0.1. Hence, the flux of the excited atoms to the cathode surface must be of the order of 10% of the ion flux or higher for the electron emission from impact of excited atoms to be at least comparable to the electron emission from ion impact. Unfortunately, no data on flux of excited atoms to electrodes in arc plasmas seem to be available in the literature. Note that results of numerical computation of the excited atom density in atmospheric-pressure arcs are reported in a number of works, e.g. [5, 15, 31], however, it is difficult to draw definite conclusions from these results. (For example, the excited atom density near the cathode, computed in [5], is by a factor of at least 300 lower that the ion density. Therefore, for the electron emission from the impact of excited atoms to be at least comparable to the electron emission from ion impact, the diffusion speed of excited atoms should exceed the drift speed of ions by at least 30 times, a possibility that appears unlikely.)

In this connection, another (auxiliary) model of argon plasma was built that took into account ions, electrons, and atoms in the ground state and an effective excited state. The kinetic and transport coefficients were the same as in the model of atmospheric-pressure corona discharge supplied with the Plasma module of COMSOL Multiphysics® [21] as a part of the application library, with the Stefan–Maxwell equations replaced by the drift-diffusion equations. The boundary condition for the excited atom density at the electrode surfaces was similar to (5). An example of the results given by this model is shown in figure 3. The density of excited atoms in the near-cathode space-charge sheath exceeds the ion density by an order of magnitude or more; however, the ion flux is about an order of magnitude higher than the flux of excited atoms. Note that the ion drift speed exceeds the diffusion speed of excited atoms by about two orders of magnitude. If the secondary emission coefficients of excited atoms are of order unity, then the electron emission current from the impact of excited atoms is comparable to the ion-electron emission current.

One can conclude that the electron emission from the impact of excited atoms can hardly be a dominant effect. However, it may still be of the same order as the ion-electron emission, in which case it will affect the current transfer to cold cathodes, as shown in the preceding section.

In the numerical model described in section 2, the electron emission from the impact of excited atoms is accounted for jointly with the other secondary electron emission mechanisms due to ion and photon bombardment in terms of a single effective secondary emission coefficient γ. This approximation is usual in the modelling of cold discharges (e.g. section
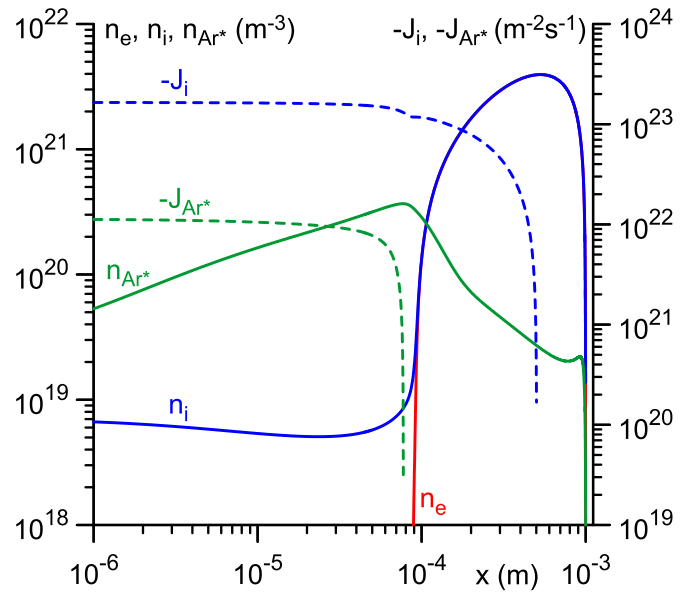

Figure 3. Distributions of the densities of ions, electrons, and excited atoms and of the densities of fluxes of the ions and excited atoms in the direction towards the cathode. $\gamma = 0.1$, $h = 1$ mm, $T_c = T_a = 1500$ K, $j_c = 3 \times 10^4$ A m^{-2}.

4.7.2 of [25]) and stems from the fact that individual emission coefficients are usually known at best in order of magnitude. If the effect of electron emission from the impact of excited atoms were dominant, it would be reasonable to improve the model of section 2 by introducing an allowance for excited atoms as separate species, as is done in the auxiliary model described in the current section, and by characterizing the electron emission from the impact of excited atoms by an individual emission coefficient. However, secondary electron emission due to excited species bombardment can hardly be a dominant effect, as shown above, and such an improvement does not seem useful at this stage. Therefore, the model described in section 2 is employed in the rest of this work.

5. Arc ignition on cold electrodes

The results reported in this section refer to processes in the plasma coupled with heat propagation inside the electrodes and have been obtained by means of numerical solution of the full system of equations described in section 2.1, supplemented with the boundary conditions (3)–(11). The reported results refer to the atmospheric-pressure argon plasma, electrodes made of tungsten or copper, the temperatures at the bottom of the electrodes $T_{s1} = T_{s2} = 300$ K, and the effective secondary electron emission coefficient $\gamma = 0.1$. The temperature-dependent mass density ρ_s, isobaric specific heat C_{ps}, and thermal conductivity κ_s have been taken from [32] for tungsten and from [33–35], respectively, for copper. (C_{ps} was corrected to include the latent heat of melting.) Simulation results are reported for the case of AC arc current $j_c(t) = 5 \times 10^7$ A m$^{-2} \sin(100\pi$ Hz$t)$. The simulations were initiated at $t = 0$ with the initial conditions $n_e = n_i = 10^{16}$ m^{-3}, $T_h = T_s = 300$ K, $T_e = 20 \times 10^3$ K, $\varphi = 0$. In order to investigate the
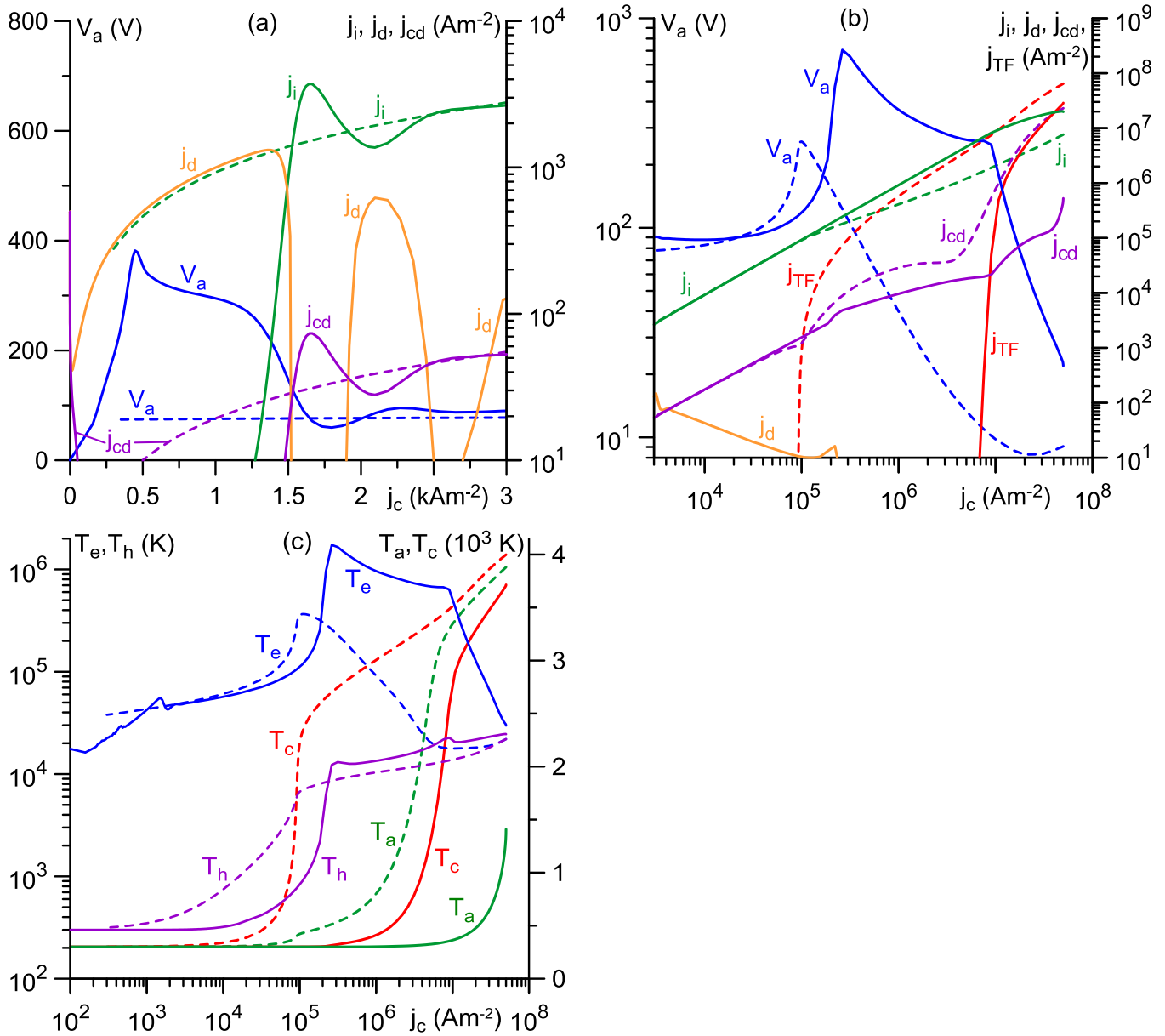
Figure 4. (a), (b) Discharge voltage and various components of electric current to the cathode surface. (c) Maximum values of the electron and heavy-particle temperatures in the gap and temperatures of the electrode surfaces. Solid: AC modelling. Dashed: quasi-stationary modelling. $h = 1$ mm.

'inertia' of the system, the simulation results for each t or, equivalently, each value of the instantaneous current density j_c are compared with the results of quasi-stationary simulations performed with a (constant) current density equal to j_c.

5.1. Variations of integral characteristics of the discharge

Let us first consider results for the case where the electrode material is tungsten and the electrode thicknesses h_1 and h_2 are equal to 1 cm. The computed variations of integral characteristics of the discharge for the gap $h = 1$ mm are shown in figure 4. The results of the (time-dependent) AC modelling in this and subsequent figures are shown as functions of the instantaneous value of electric current j_c (instead of time),

in order to facilitate a comparison with results of the quasi-stationary modelling as described in the previous paragraph. $j_d = -\varepsilon \, \partial E/\partial t|_{x=0}$ is the density of displacement current to the cathode surface, and $j_{cd} = e \, n_e C_e/4|_{x=0}$ is the modulus of the density of current transported to the cathode surface by plasma electrons counterdiffusing against the electric field. We note for convenience that $j_c = (1 + \gamma) j_i + j_{TF} - j_{cd} + j_d$.

Figures 4(a) and (b) illustrate mechanisms of current transfer to the cathode. Note that the quasi-stationary modelling was performed for j_c starting from 300 A m^{-2}; numerical difficulties arose for lower j_c and the effort that would be required to overcome it was considered unwarranted since this range does not appear to be of physical relevance. It is seen from figure 4(a) that there is a significant plasma electron current j_{cd}

during a brief period of time immediately after the arc ignition, $j_c \lesssim 100$ A m^{-2} or, equivalently, $t \lesssim 6$ ns. This current is virtually compensated by the displacement current j_d. After this period, j_{cd} is virtually zero and the current transfer to the cathode is dominated by the displacement current j_d. At $j_c \approx 1.4 \times 10^3$ A m^{-2} or, equivalently, $t \approx 89$ ns j_d attains a maximum value of approximately 1.3 kA m^{-2}. After the maximum, j_d rapidly decreases and is overtaken by the ion current j_i. Interestingly, the decay of the displacement current is oscillatory; note that j_d in the ranges 1.5 kA m$^{-2} \lesssim j_c \lesssim 1.9$ kA m^{-2} and 2.5 kA m$^{-2} \lesssim j_c \lesssim 2.7$ kA m^{-2} is negative and not represented on the graph. The ion current remains the dominant mechanism of current transfer until $j_c \approx 10^7$ A m^{-2}, when the electron emission current j_{TF} comes into play; figure 4(b). In the quasi-stationary case, the electron emission comes into play for significantly lower j_c values, of the order of 10^5 A m^{-2}. Note that the electron emission is of thermionic nature in these conditions both in the AC and quasi-stationary cases. While for $j_c = 5 \times 10^7$ A m^{-2} the thermionic emission current exceeds the ion current by an order of magnitude in the quasi-stationary case, the two currents are close in the AC case.

Immediately after the arc ignition (figure 4(a)), the discharge voltage V_a rapidly increases and attains a maximum value of approximately 390 V at $j_c \approx 0.45$ kA m^{-2}, i.e. in the current range where the displacement current is dominant. Note that V_a in this region is sensitive to the initial conditions, i.e. the height of the maximum decreases as the initial charged particle density increases. After the maximum, V_a decreases and in the range $j_c \gtrsim 1.6$ kA m^{-2} becomes close to the quasi-stationary value of the discharge voltage, which is virtually constant in this range at approximately 80 V.

Both AC and quasi-stationary discharge voltages remain close to 80 V up to $j_c \approx 4 \times 10^4$ A m^{-2}, after which they start increasing, with the quasi-stationary voltage increasing a bit faster; see figure 4(b). In the quasi-stationary case, V_a passes through a maximum of approximately 260 V at $j_c \approx 10^5$ A m^{-2}, which is where the thermionic emission comes into play, and starts decreasing, eventually reaching values in the range 10–20 V, which are typical of arc discharges. This is a quasi-stationary scenario of transition from the abnormal glow discharge to the arc discharge, which is well known in the gas discharge theory (e.g. figure 279 in [36] and figures 8.4 and 10.1 in [25]) and was studied by means of similar 1D quasi-stationary modelling in [11, 15, 16] and by means of 2D quasi-stationary modelling in [10].

The AC case is different. The maximum in V_a is higher, $V_a \approx 700$ V, occurs at a higher current, $j_c \approx 2.5 \times 10^5$ A m^{-2}, and, most importantly, is unrelated to the electron emission, which becomes appreciable only at much higher currents, close to 10^7 A m^{-2}. The analysis of the distributions of the ion current density, similar to the ones depicted in figure 2, shows that the contribution of the cathode sheath to the total ion current is appreciable before the maximum and negligible after the maximum. In other words, the maximum is governed by the same mechanisms as the turning point separating the lower and intermediate sections of the S-shapes

shown in figure 1. V_a monotonically decreases after the maximum, with a rapid change of slope occurring around $j_c \approx 10^7$ A m^{-2}, where thermionic emission comes into play. Eventually, V_a attains values of the order of 20 V, typical for arc discharges. One can conclude that the glow-to-arc transition in the AC case occurs in a way substantially different from the quasi-stationary one.

The evolution of the maximum values of the electron and heavy-particle temperatures in the gap and of the temperatures of the electrode surfaces is shown in figure 4(c). Note that the maximum electron temperature occurs in the near-cathode space-charge sheath, except for low j_c where the sheaths have not yet been formed. It is seen that T_e may be very high, of the order of 100 eV. Note also that the analysis shows that the term of the electron energy equation involving the time derivative is small except for $t \lesssim 10$ ns.

It is seen from figure 4(c) that the values of the maximum electron temperature in the AC case are close to the corresponding quasi-stationary values in the range of j_c from approximately 10^3–3×10^4 A m^{-2}. The AC values are below the quasi-stationary ones in the range 3×10^4 A m$^{-2} \lesssim j_c \lesssim 2 \times 10^5$ A m^{-2} and exceed the latter for higher j_c. In the quasi-stationary case, the dependence $T_e(j_c)$ attains a maximum at $j_c \approx 10^5$ A m^{-2}. The AC dependence attains a maximum at $j_c \approx 2.7 \times 10^5$ A m^{-2} and reveals a fast change of slope at j_c about 10^7 A m^{-2}. All these features are in broad agreement with the corresponding features of variations of the AC and quasi-stationary discharge voltage values, as discussed above.

It is seen from figure 4(c) that in the quasi-stationary case the heavy-particle gas starts being heated at lower values of j_c than the electrodes, which should have been expected since the thermal conductivity of the gas is significantly lower than that of the electrode metal. The quasi-stationary temperature of the cathode surface is higher than the anode temperature for $j_c \lesssim 10^7$ A m^{-2} and the two temperatures are close to each other for higher j_c. Obviously, a similar relation exists between the quasi-stationary values of the densities of the energy fluxes to the electrodes. In the AC case, the heavy-particle gas and each of the electrodes start being heated at significantly higher current densities than in the quasi-stationary case, which should have been expected and is a manifestation of thermal inertia. As a consequence, the AC anode temperature does not exceed 1500 K during the modelling time (5 ms).

The computed variations of integral parameters of the discharge for the gap widths $h = 100\ \mu$m and 1 cm are shown in figures 5 and 6. It is seen from figures 4(a) and 5 that the height of the first maximum in the variation of the AC discharge voltage, which occurs in the range of low j_c values where the current transfer to the cathode is dominated by the displacement current, increases with increasing gap width. It is seen from figures 4(b) and 5 that the second maximum in all three h values occurs at j_c several times 10^5 A m^{-2}, has a height of approximately 700 V, and is followed by a rapid change of the slope. However, the shape of the second maximum is not the same; the maximum is rather wide for $h = 100\ \mu$m and relatively narrow for $h = 1$ mm and 1 cm.

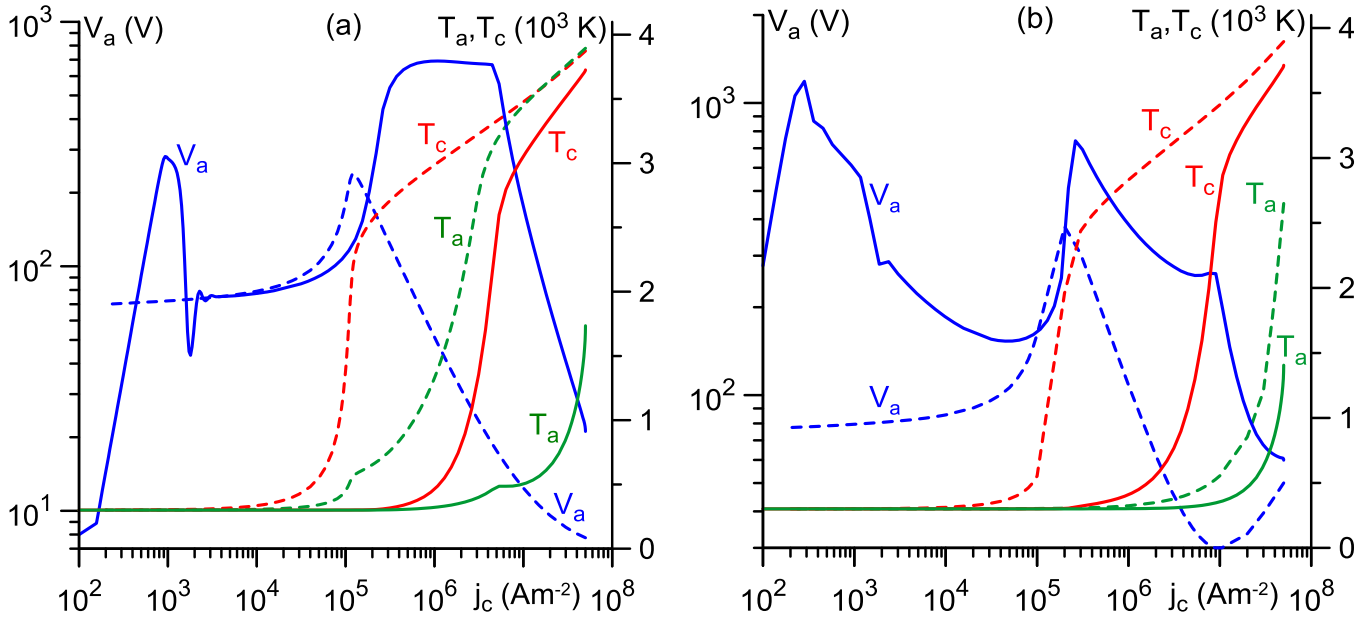J. Phys. D: Appl. Phys. **54** (2021) 195202

D F N Santos *et al*

Figure 5. Discharge voltage and temperatures of the electrode surfaces. Solid: AC modelling. Dashed: quasi-stationary modelling. (a) $h = 100\,\mu$m. (b) $h = 1$ cm.
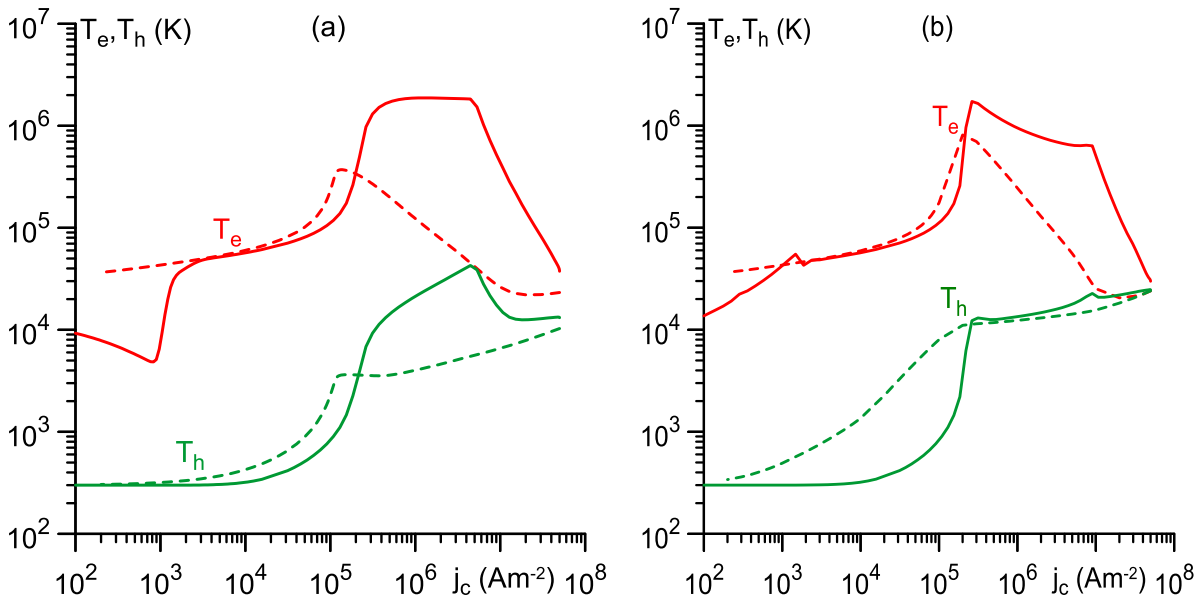

Figure 6. Maximum values of the electron and heavy-particle temperatures in the gap. Solid: AC modelling. Dashed: quasi-stationary modelling. (a) $h = 100\,\mu$m. (b) $h = 1$ cm.

It is seen from figures 4(c) and 5 that the gap width does not very strongly affect the AC variations of the electrode surface temperatures. On the other hand, there is a significant effect over the quasi-stationary variation of the anode surface temperature; while T_a for $j \gtrsim 10^7$ A m^{-2} is around 3500 K or higher and close to T_c for $h = 100\,\mu$m and 1 mm, it does not exceed approximately 2700 K for $h = 1$ cm.

The AC and quasi-stationary variations of the maximum value of the electron temperature in the gap for $h = 100\,\mu$m and 1 cm (figure 6) are broadly similar to the discharge voltage variations, as is the case for $h = 1$ mm as discussed above. An exception is the range $j_c \lesssim 10^3$ A m^{-2} in the case

$h = 100\,\mu$m, where the AC electron temperature decreases with increasing j_c. It is seen from figures 4(c) and 6 that the variations of the maximum value of the heavy-particle temperature in the gap are not strongly affected by the gap width.

5.2. Distributions of parameters in the gap

Representative examples of distributions of parameters in the gap are shown in figure 7 for different values of j_c. The quasi-neutral bulk plasma and a thin near-cathode space-charge sheath are seen in all cases except in the AC modelling for
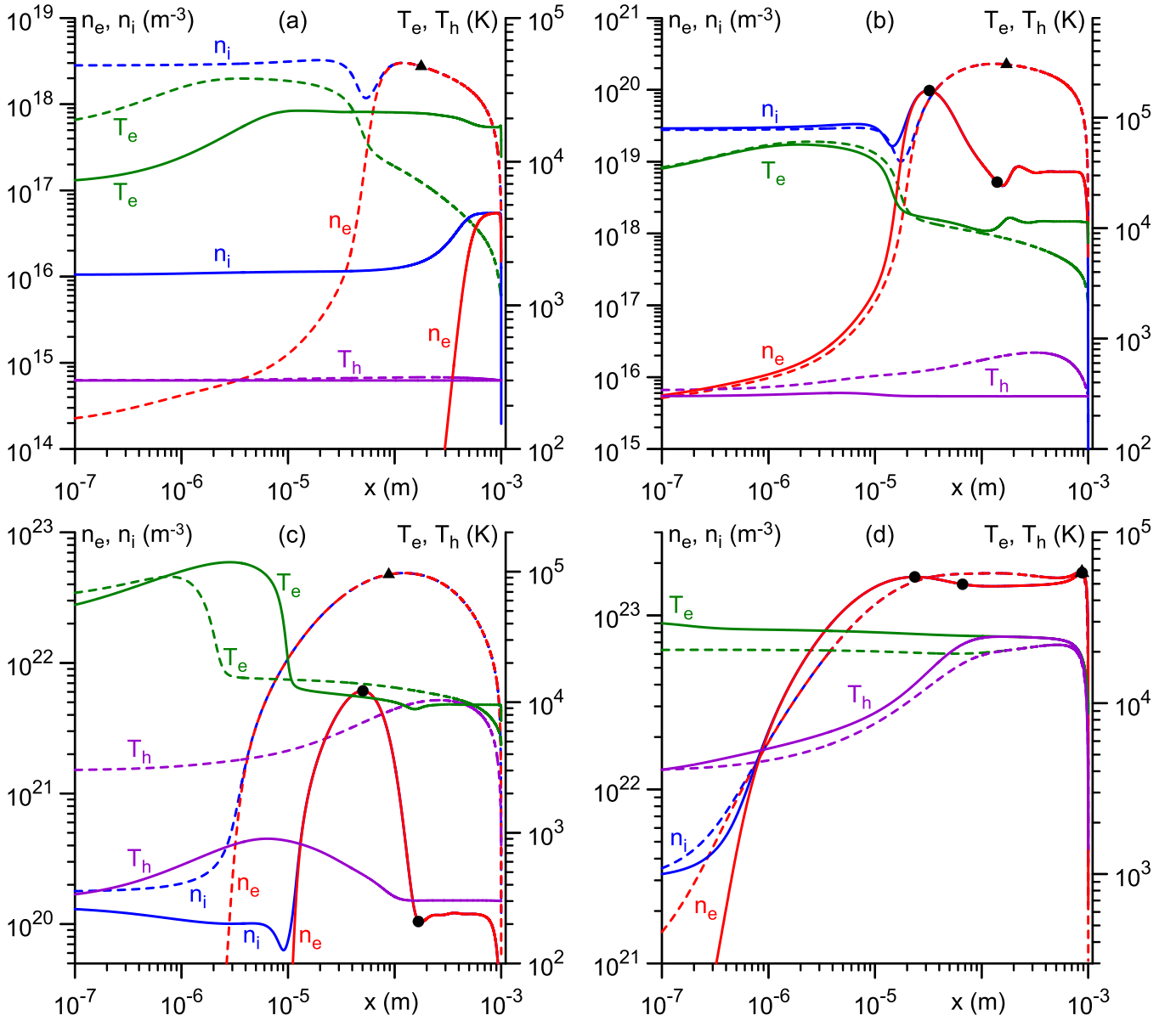
Figure 7. Lines: distributions of parameters in the gap. Circles, triangles: points of reversal of the electric field. Solid circles: AC modelling. Dashed triangles: quasi-stationary modelling. The circle in the near-anode region in figure (d) coincides with a triangle. $h = 1$ mm. $j_c = 300\,\mathrm{A\,m^{-2}}$ (a), $10^4\,\mathrm{A\,m^{-2}}$ (b), $10^6\,\mathrm{A\,m^{-2}}$ (c), $5 \times 10^7\,\mathrm{A\,m^{-2}}$ (d).

$j_c = 300$ A m^{-2} (figure 7(a)), where the space-charge sheath is not thin.

In the AC case, figure 7(a) refers to 19 ns. The electric field at the cathode surface is 3×10^5 V m^{-1}, and the mobilities of the ions and electrons are of the order of 10^{-4} m^2 V^{-1} s^{-1} and 1 m^2 V^{-1} s^{-1}, respectively. The drift times of the ions and the electrons over the distance of 0.5 mm are of the order 17 μs and 1.7 ns, respectively. This is consistent with the near-cathode space-charge sheath being electron-free with n_i close to its initial value of 10^{16} m^{-3}.

The AC heavy-particle temperature T_h remains close to its initial value of 300 K in figures 7(a)–(c) except in the near-cathode region, $x \lesssim 0.1$ mm, in figure 7(c). Thus, heating of the heavy particles is the slowest process, as should have been expected. The AC distributions of all parameters are close to

their quasi-stationary counterparts in the near-cathode region in figure 7(b) and in the whole gap in figure 7(d).

Thermal equilibrium $T_h \approx T_e$ holds in the bulk plasma in the quasi-stationary case in figure 7(c) and in both the quasi-stationary and AC cases in figure 7(d). It is interesting to note that the distribution of the electron temperature is virtually uniform in figure 7(d) in both the AC and quasi-stationary cases, except in the vicinity of the anode.

The distribution of the electric field in the gap is shown in figure 8 for $j = 5 \times 10^7$ A m^{-2}. An interesting feature of this figure is the reversals (changes of direction) of the electric field. Distributions of the electric field for other j values are skipped in order not to increase the paper volume; however, it should be stressed that there are field reversals as well. For convenience, the field reversals are shown in figure 7.
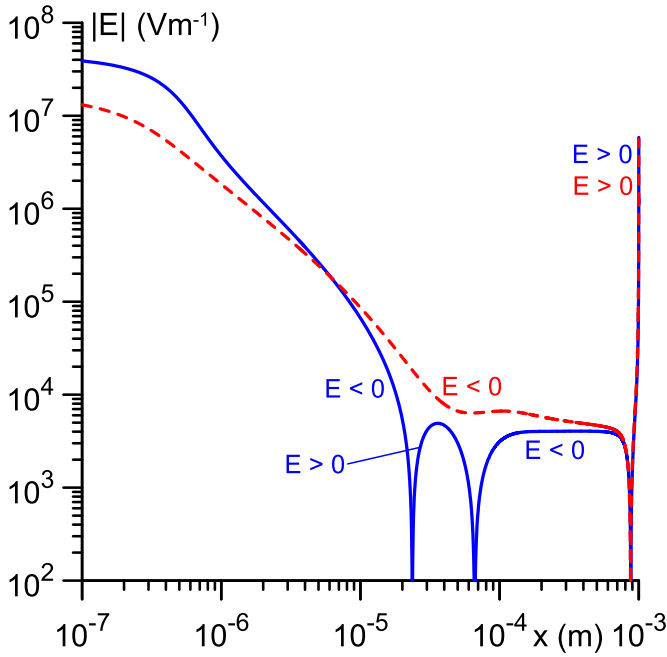
Figure 8. Distribution of modulus of the electric field in the gap. Solid: AC modelling. Dashed: quasi-stationary modelling. $h = 1\,\text{mm}$, $j_c = 5 \times 10^7\,\text{A m}^{-2}$.
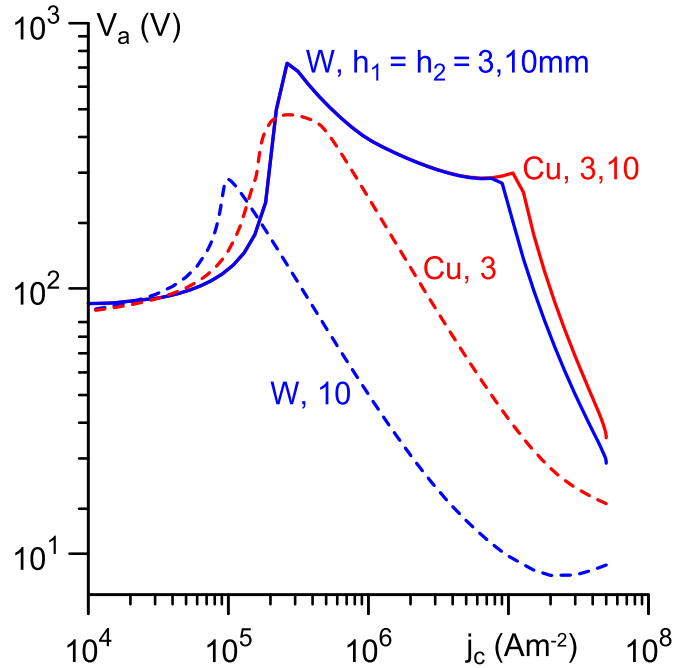

Figure 9. Discharge voltage for tungsten and copper electrodes of various thicknesses. Solid: AC modelling. Dashed: quasi-stationary modelling. $h = 1\,\text{mm}$.

In most cases, the field reversals occur near extrema of the charged particle distribution. There is one field reversal in the quasi-stationary case in each of figures 7(a)–(d), with the reversal point being positioned at distances of the order of 0.1 mm from the cathode in figures (a)–(c) and at a distance of the order of 0.1 mm from the anode in figure (d). Thus, the quasi-stationary electric field in near-electrode regions of thickness of the order of 0.1 mm is directed to the electrode in all the cases (i.e. $E < 0$ near the cathode and $E > 0$ near the anode) and the quasi-stationary electric field in the bulk plasma is directed to the anode for $j_c \lesssim 10^6\,\text{A m}^{-2}$ and to the cathode for $j_c = 5 \times 10^7\,\text{A m}^{-2}$. In other words, there is a pronounced negative anode voltage in the quasi-stationary case for $j_c = 5 \times 10^7\,\text{A m}^{-2}$.

In the AC case, the electric field in figure 7(a) is directed to the cathode in the whole gap. There are two AC field reversals in figures 7(b) and (c). There are three AC field reversals in figure 7(d) (see also figure 8), with one of them occurring at a distance of the order of 0.1 mm from the anode. Thus, the anode voltage in the AC case is negative for $j_c = 5 \times 10^7\,\text{A m}^{-2}$, as it is in the quasi-stationary case.

5.3. Effect of electrode material and thickness

Figure 9 shows the discharge voltage, evaluated for electrodes of thicknesses of 3 and 10 mm made of tungsten and copper. The lines depicting the AC discharge voltage for the tungsten electrodes of the two thicknesses coincide to the graphical accuracy, and the same is true for the copper electrodes. Moreover, the effect of the electrode material on the AC discharge voltage is virtually inexistent until the arc current has reached values of the order of $10^7\,\text{A m}^{-2}$, and even then the

effect is minor. In contrast, the effect of the electrode material and thickness on the quasi-stationary discharge voltage is significant, as exemplified by the two dashed lines.

The absence of the effect of the electrode thicknesses in the AC case suggests that the heat propagation length over the considered time interval (5 ms) is smaller than 3 mm, and this is indeed the case as illustrated by figure 10. Note that in this example the computed temperature of the surface of both tungsten and copper cathodes in both AC and quasi-stationary cases, as well as the anode surface temperature in the quasi-stationary case, exceeds 3500 K and is significantly higher than the boiling temperature of copper (2835 K). Therefore, the computation results for copper serve for illustrative purposes only. This point will be discussed in some detail in the Conclusions.

6. Effect of field to thermo-field emission

It is well known that current–voltage characteristics of field electron emission from cold cathodes in a vacuum approximately follow the Fowler–Nordheim formula with the applied electric field being multiplied by the so-called field enhancement factor β, which is of the order of 10^2 or higher; e.g. [37, 38]. Various mechanisms for the enhancement have been postulated, such as geometrical 'tips' and suppressed work function, but there is rarely independent confirmation; e.g. [39]. It was found in the modelling of low-current (around 30 mA) gliding arcs in atmospheric-pressure argon [8] that the effect of field electron emission taking account of the enhanced electric field may have a considerable impact on the cathode fall and the discharge power.
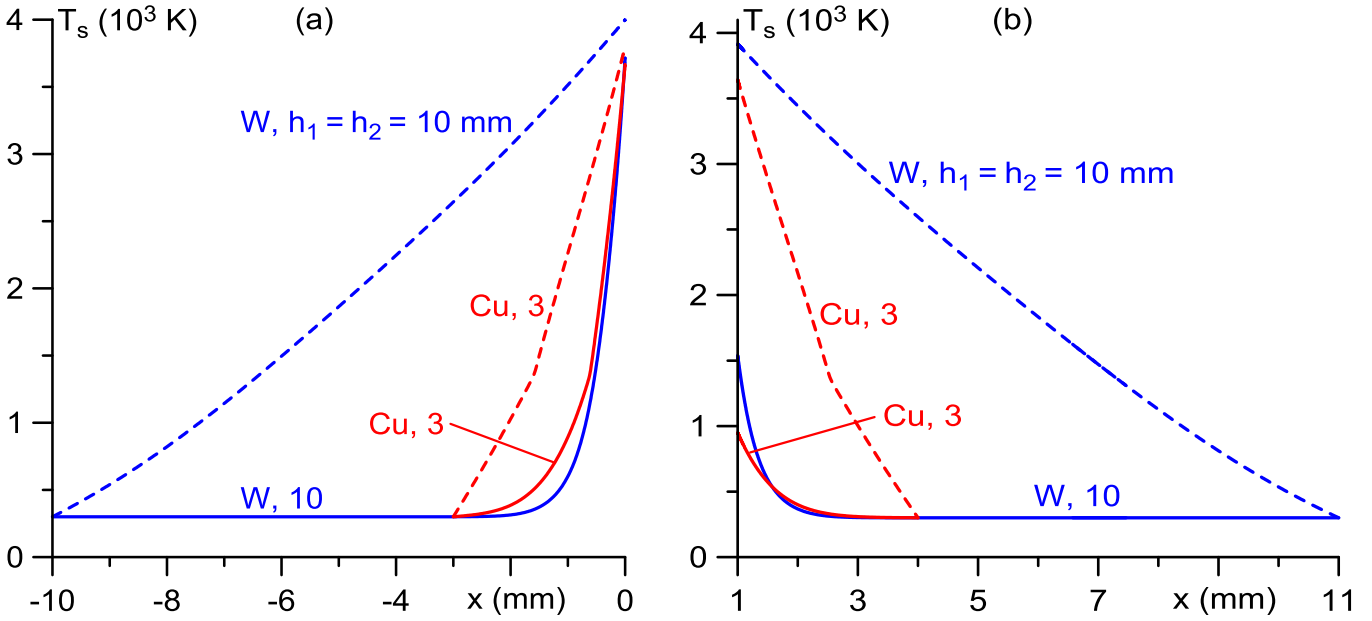
Figure 10. Distribution of temperature inside the cathode (a) and the anode (b). Tungsten and copper electrodes of thicknesses 3 and 10 mm. Solid: AC modelling. Dashed: quasi-stationary modelling. $j_c = 5 \times 10^7 \, \mathrm{A\,m^{-2}}$, $h = 1$ mm.
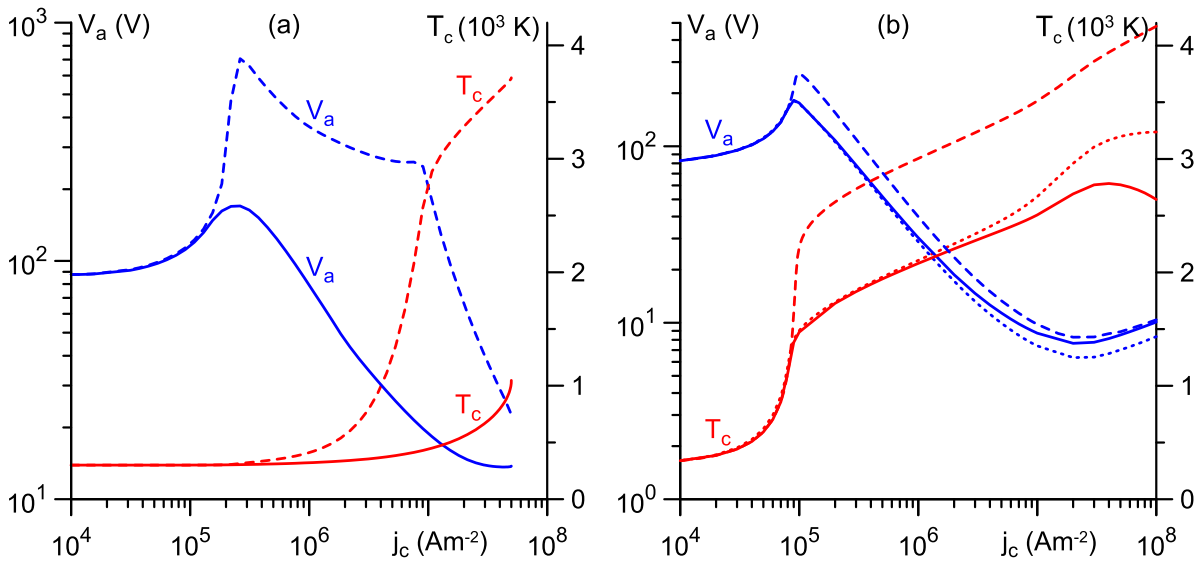

Figure 11. Effect of field enhancement on the discharge voltage and cathode surface temperature. (a) AC modelling. (b) Quasi-stationary modelling. $h = 1$ mm. Solid: $\beta = 100$. Dashed: $\beta = 1$. Dotted: see text.

Figure 11(a) illustrates the effect of field electron emission with accounting for the enhanced electric field on the evolution of the discharge voltage and cathode surface temperature during ignition of the discharge on cold electrodes with a subsequent transition to the arc. Figure 11(b) depicts the quasi-stationary case. Both figures refer to the tungsten electrodes of thicknesses $h_1 = h_2 = 1$ cm. In these simulations, the density j_{TF} of field to thermo-field to thermionic electron emission current was evaluated in terms of the cathode surface temperature T_c and the electric field at the cathode surface equal to $\beta \left(- E|_{x=0} \right)$, where β is the field enhancement factor and $\left(- E|_{x=0} \right)$ is the modulus of the electric field obtained from the solution of the differential equations described in section 2.1,

or, in other words, of the field induced by the near-cathode space-charge sheath. The dashed lines in figure 11, which refer to $\beta = 1$ and correspond to no field enhancement, have been computed with the emission current density j_{TF} determined by means of the Murphy–Good formalism or the Richardson–Schottky formula (see section 2.2); no difference was detected in the results. The Murphy–Good formalism was used for the computation of the solid lines, referring to $\beta = 100$.

One can see from figure 11 that the effect of enhancement by a factor of 100 comes into play for j_c of the order of 10^5 A m^{-2} in both AC and quasi-stationary cases and results in a reduction of both the discharge voltage and the cathode temperature. In particular, the cathode surface temperature

remains below 2800 K for all j_c values even in the quasi-stationary case.

Note that the WKB approximation used in the Murphy–Good formalism [28] will become poor for extremely high electric field strengths of the order of 10^{10} V m^{-1} or higher [40–42]. However, values that high have not been encountered in the calculations; the enhanced electric field for $\beta = 100$ remained below 4×10^9 V m^{-1}.

The boundary condition (10) is written using the assumption that an electron leaving the electrode surface carries away, in addition to thermal energy, energy equal to the work function A_f. However, the electron energy may be reduced compared to A_f due to the presence of a strong electric field directed towards the cathode surface. If the electron emission from the cathode occurs in the thermionic regime, the reduction amounts to the Schottky correction, which is much smaller than A_f. However, if the electron emission occurs in the thermo-field or field emission regimes, then the reduction may be significant. It may even exceed A_f, which would mean that the electron emission contributes to heating of the cathode: the Nottingham effect.

In this connection, simulations have been performed with A_f in the boundary condition (10) at the cathode surface being replaced with the energy evaluated in terms of the cathode surface temperature and the local electric field (multiplied by β) by means of fit formulas [40]. Note that the other boundary conditions at the cathode surface remained unchanged, which may be not quite correct as discussed in the appendix of [43]; however, it is sufficient for an estimate. The results of simulations performed in this way in the quasi-stationary case for $\beta = 100$ are shown by the dotted lines in figure 11(b). It is seen that the cathode surface temperature for $j_c \gtrsim 10^6$ A m^2 is somewhat higher than the temperature shown by the solid line (which was computed with the use of the original boundary condition (10), written in terms of A_f), and attains approximately 3250 K.

The value $\beta = 100$ is at the lower end of the range of enhancement factor values considered in the literature; e.g. values of β in the range 150–350 are cited in [37] and values from 100 to 1000 are considered in [8]. An increase in β causes a decrease in the computed cathode surface temperature. Typical current densities for this type of arc are in the range 10^7–10^8 A m^{-2}; e.g. [4]. Thus, the cathode surface temperature, computed taking account of field to thermo-field emission with electric field enhancement at the cathode surface, does not exceed values around 3000 K even in the quasi-stationary case over the entire range of relevant current densities and enhancement factor values considered in the literature. Since the melting temperature of tungsten is appreciably higher (approximately 3700 K), this would mean that pure tungsten cathodes of atmospheric-pressure argon arcs can operate without melting. It is well known from the experiment that the latter is not the case.

One can conclude that the introduction of the electric field enhancement on cathodes of arc discharges leads to a contradiction with experiments. This suggests that the enhancement of the electric field has no effect on electron emission from the cathodes of arc discharges, in contrast to what occurs in field

emission experiments in a vacuum. A possible reason is the conditioning effect produced on the cathode surface by high ion fluxes, which are necessary to create strong electric fields on the surface.

7. Summary and concluding remarks

Since the experiment cannot clarify the mechanism of current transfer to non-thermionic arc cathodes, this can only be done by means of numerical modelling that is based on first principles and does not rely on *a priori* assumptions on physical mechanisms that are dominant in different discharge regions. The most general approach to modelling high-pressure arc plasmas is so-called unified modelling, where a single set of differential equations, comprising conservation and transport equations for all plasma species, the electron and heavy-particle energy equations, and the Poisson equation, is solved in the whole interelectrode gap up to the electrode surfaces. This approach allows one to describe, in a natural way, the whole process of an AC arc development, including the switching of polarity, until the periodic regime has been reached. In this work, results are reported of the unified 1D modelling of the first quarter-period after the ignition of an AC arc between cold electrodes in atmospheric-pressure argon. The results are compared with those for DC discharges and analysed with the aim of clarifying the roles of different mechanisms of current transfer to non-thermionic arc cathodes.

A numerical model used to this end necessarily takes into account substantially different physical processes occurring on different time and space scales and therefore involves many transport and kinetic coefficients, not all of which are known well. Nevertheless, the overall accuracy of the modelling should be sufficient at least for qualitative conclusions.

The current transported to the surface of a cold cathode by ions diffusing from the bulk of atmospheric-pressure arcs may reach an order of magnitude of 10^7 A m^{-2} for high values of the discharge gap width and/or secondary electron emission coefficient;, however, this would require very high discharge voltage, of several hundred volts. The reason the voltages are that high is that the ion current is limited not by a finite ion diffusion rate but rather by the lack of ionization energy in the near-cathode region: the ionization energy is provided by work of the sheath electric field on electrons emitted by the cathode surface, similarly to the case of thermionic cathodes; since the electron emission current from cold cathodes is low (secondary emission only), a very high sheath voltage is needed to provide sufficient ionization energy. This conclusion is also relevant to the analysis of diffuse attachments of vacuum arcs to hot cathodes; cf [30].

The first quarter-period after the ignition of an AC arc on cold electrodes is investigated numerically for the case of a 50 Hz arc with an amplitude of current density of 5×10^7 A m^{-2}. As seen from the data on various components of electric current to the cathode surface shown in figures 4(a) and (b) and similar data for the gap widths $h = 100$ μm and 1 cm, which are skipped for brevity, the displacement current is the dominating mechanism for $j_c \lesssim 1.5 \times 10^3$ A m^{-2}. The

ion current comes into play at higher j_c and remains the dominant mechanism of current transfer until j_c reaches values of the order of 10^7 A m^{-2}. The secondary electron emission current is low; however, it plays an important role in providing energy for ionization in the near-cathode region. Starting from arcing times of about 0.5–1 ms (note that the value $j_c = 10^7$ A m^{-2} is attained at $t = 0.65$ ms), thermionic electron emission from the cathode comes into play and at $t = 5$ ms becomes approximately equal to the ion current.

The glow-to-arc transition in the AC case occurs in a way substantially different from the well-known quasi-stationary scenario of the glow-to-arc transition. In the quasi-stationary case, the current density–voltage characteristic $V_a(j_c)$ passes through a maximum of about 200–400 V, depending on the gap width, at j_c of the order of 10^5 A m^{-2}, when the thermionic emission comes into play. In the AC case, the maximum of the dependence $V_a(j_c)$ is higher, of the order of 700 V, and is unrelated to the electron emission, which becomes appreciable only at much higher current densities. The analysis of the spatial distribution of the ion current density shows that the contribution of the cathode sheath to the total ion current is appreciable before the maximum and negligible after the maximum. The discharge voltage monotonically decreases after the maximum, with a rapid change of slope occurring when the thermionic emission comes into play at j_c of the order of 10^7 A m^{-2}.

The AC discharge voltage is not appreciably affected by the electrode material and thicknesses. The absence of the effect of the electrode thicknesses is consistent with the heat propagation length over the considered time interval (5 ms) being smaller than 3 mm. The cathode surface is heated up to approximately 3720 K. The anode surface is heated up to approximately 1000–1500 K, depending on conditions.

Since the computed temperature of copper cathodes and, in the quasi-stationary case, of anodes also significantly exceeds the boiling temperature of copper, the vaporization of copper needs to be taken into account. Therefore, the computation results for copper serve illustrative purposes only.

It was pointed out in [44] that the weld pools in gas metal arc welding of steel are never observed to be boiling. It was assumed on this basis that the energy flux from the plasma to the cathode surface vanishes as the surface temperature approaches the boiling temperature, because of lowering of the local plasma temperature due to cold metal vapour. It would be very interesting to introduce the cathode metal vaporization into the unified numerical model used in this work or similar, and to accurately investigate this point.

Thus, the dominant mechanisms of current transfer to (non-thermionic) cathodes during AC arc ignition between cold electrodes are, subsequently, the displacement current, the ion current, and thermionic emission current. No indications of explosive emission were found, an unsurprising result given that recent numerical modelling of the formation of cathode spots in vacuum arcs [45–50] and of unipolar arcs [51] has not detected microexplosions either. The electron emission from the impact of excited atoms can hardly be a dominant mechanism either.

The electric field at the cathode surface, induced by the near-cathode space-charge sheath, is clearly insufficient for appreciable field or thermo-field emission. On the other hand, the cathode surface temperature, computed taking account of field to thermo-field emission with electric field enhancement at the cathode surface due to surface micrononuniformities, is substantially lower than the melting temperature of tungsten even in the quasi-stationary case over the entire range of relevant current densities and enhancement factor values considered in the literature. This would mean that pure tungsten cathodes of atmospheric-pressure argon arcs can operate without melting. It is well known from the experiment that the latter is not the case. Thus, the enhancement of the electric field, apparently, has no effect on electron emission from cathodes of arc discharges, in contrast to what occurs in field emission experiments in a vacuum. A possible reason is the conditioning effect produced on the arc cathode surface by high ion fluxes, which are necessary to create strong electric fields on the surface.

The results of application of the analysis of this work to operation of low-voltage circuit breakers will be reported in a forthcoming publication.

Appendix A. Species conservation and energy equations in non-equilibrium arc plasmas

Let us consider a multicomponent ideal gas mixture and designate by m_α, n_α, $\rho_\alpha = m_\alpha n_\alpha$, and $\mathbf{v}_\alpha$ the particle mass, the number density, the mass density, and the mean velocity of particles of species α. The mass density and mean mass velocity of the mixture are expressed as $\rho = \sum_\alpha n_\alpha m_\alpha$, $\mathbf{v} = \rho^{-1} \sum_\alpha \rho_\alpha \mathbf{v}_\alpha$. The diffusion (transport) velocity and the transport flux of the species α are $\mathbf{V}_\alpha = \mathbf{v}_\alpha - \mathbf{v}$, $\mathbf{J}_\alpha = n_\alpha \mathbf{V}_\alpha$. Note that

$$\sum_\alpha \rho_\alpha \mathbf{V}_\alpha = 0. \tag{12}$$

Equations of conservation of particle number, momentum, and energy of each species are obtained by means of the well-known procedure of integration of the species Boltzmann equation with appropriate weights; e.g. [20, 52]. In particular, the equations of conservation of particle number and energy of species α may be written as

$$\rho \frac{d}{dt}\left(\frac{n_\alpha}{\rho}\right) + \nabla \cdot (n_a \mathbf{V}_\alpha) = w_\alpha, \tag{13}$$

$$\rho \frac{d}{dt}\left(\frac{\rho_\alpha}{\rho}u_\alpha\right) = -\nabla \cdot \mathbf{q}_\alpha - p_\alpha \nabla \cdot \mathbf{v} + \hat{\boldsymbol{\tau}}_\alpha : (\nabla \mathbf{v})$$
$$+ \rho_\alpha \mathbf{V}_\alpha \cdot \left(\mathbf{F}_\alpha - \frac{d\mathbf{v}}{dt}dt\right) - \sum_\beta R^{(e)}_{\alpha\beta} + W^{(e)}_\alpha.$$

$$(14)$$

Here, $d/dt = \partial/\partial t + \mathbf{v} \cdot \nabla$ is the material derivative; u_α, $\mathbf{q}_\alpha$, p_α, and $\hat{\boldsymbol{\tau}}_\alpha$ are the thermal energy per unit mass, the density of thermal energy flux, the hydrostatic pressure, and the viscous stress tensor of species α, respectively; $\mathbf{F}_\alpha$ is the force per unit mass acting on a particle of species α (it is assumed that this force does not depend on the particle velocity); $R^{(e)}_{\alpha\beta}$ is the rate of loss per unit volume of energy of species α due to elastic collisions with particles of species β; and w_α and $W^{(e)}_\alpha$ are rates of change of, respectively, the number density and the energy of species α due to reactions. Note that $p_\alpha = \frac{2}{3}\rho_\alpha u_\alpha$ and $R^{(e)}_{\alpha\beta} = -R^{(e)}_{\beta\alpha}$. For convenience, a detailed derivation of equations (13) and (14) is provided as supplementary material to this paper.

Note that the species conservation equations (13) are linearly dependent. (When these equations are multiplied by m_α and summed over α, each term vanishes. This follows from equation (12) and the equality $\sum_\alpha m_\alpha w_a = 0$, which is due to the mass conservation in reactions.) In the following, it will be convenient to transform the second term on the rhs of equation (14) with the use of the mass conservation equation for the mixture on the whole, which reads

$$\frac{d\rho}{dt} + \rho\nabla \cdot \mathbf{v} = 0. \qquad (15)$$

Let us consider the case where the mixture represents a plasma. Multiplying the species conservation equation (13) by the species charge number Z_α and the electronic charge e and summing over α, one obtains the current continuity equation. (Note that $\sum_\alpha Z_\alpha w_a = 0$ due to the charge conservation in reactions.) Making use of equation (15) and the Gauss law, one can rewrite the current continuity equation as

$$\nabla \cdot \mathbf{j} = 0, \quad \mathbf{j} = \sum_\alpha eZ_\alpha n_a (\mathbf{V}_\alpha + \mathbf{v}) + \varepsilon_0 \frac{\partial \mathbf{E}}{\partial t}, \qquad (16)$$

where $\mathbf{j}$ is the total electric current density and $\mathbf{E}$ is the electric field.

The force $\mathbf{F}_\alpha$ is expressed as $\mathbf{F}_\alpha = eZ_\alpha \mathbf{E}/m_\alpha$. The contribution of the electrons to the mass density and mean mass velocity of the plasma are negligible. Summing equations (14) over the heavy particles (index h), one obtains the equation of conservation of energy of the heavy particles:

$$\rho \frac{du_h}{dt} = -\nabla \cdot \mathbf{q}_h + \frac{p_h}{\rho}\frac{d\rho}{dt}dt + \hat{\boldsymbol{\tau}}_h : (\nabla \mathbf{v})$$
$$+ \sum_{\alpha=h} eZ_\alpha n_\alpha \mathbf{V}_\alpha \cdot \mathbf{E} + \sum_{\alpha=h} R^{(e)}_{ea} + \sum_{\alpha=h} W^{(e)}_\alpha, \qquad (17)$$

where

$$u_h = \sum_{\alpha=h} \frac{\rho_\alpha}{\rho}u_\alpha, \quad \mathbf{q}_h = \sum_{\alpha=h} \mathbf{q}_\alpha, \quad p_h = \sum_{\alpha=h} p_\alpha, \quad \hat{\boldsymbol{\tau}}_h = \sum_{\alpha=h} \hat{\boldsymbol{\tau}}_\alpha.$$

$$(18)$$

Note that $p_h = \frac{2}{3}\rho u_h$.

The equation of conservation of energy of the electrons is given by equation (14) for $\alpha = e$:

$$\rho \frac{d}{dt}\left(\frac{\rho_e}{\rho}u_e\right) = -\nabla \cdot \mathbf{q}_e + \frac{p_e}{\rho}\frac{d\rho}{dt} - en_e \mathbf{V}_e \cdot \mathbf{E} - \sum_{\alpha=h} R^{(e)}_{e\alpha} + W^{(e)}_e.$$

$$(19)$$

Note that $p_e = \frac{2}{3}\rho_e u_e$. The term accounting for work of viscous stress (the third term on the rhs of equation (14)) is small due to the smallness of the electron mass and was dropped, as well as the term proportional to $d\mathbf{v}/dt$.

It is assumed that the distribution functions of the heavy particles are maxwellian with the same temperature T_h and the distribution function of the electrons is maxwellian with a temperature T_e; a usual assumption for thermal plasmas. Then,

$$p_h = n_h kT_h, \quad u_h = \frac{3}{2}\frac{n_h kT_h}{\rho}, \quad p_e = n_e kT_e, \quad u_e = \frac{3}{2}\frac{kT_e}{m_e}, \quad (20)$$

where $n_h = \sum_{\alpha=h} n_\alpha$ is the number density of the heavy particles.

The above derivation is similar to the one given in the book [20], and the equation of energy of heavy particles, equation (17), coincides with equation (14.4-1) on p 457 of [20] as it should. However, the electron energy equation, equation (19), does not conform to equation (14.4-2) on p 457 of [20] in that the material derivative term on the lhs of the latter equation is written in the form $\rho_e du_e/dt$. For the same reason, equation (19) does not conform to the electron energy density equation implemented in the Plasma module of COMSOL Multiphysics® [21]. On the other hand, equation (19) conforms to equation (5.4) on p 189 of the book [19].

Since the transport, kinetic, and radiation coefficients of the plasma in this work are evaluated by means of formulas derived for a three-component plasma in [6], it is convenient to give relations between the quantities employed in this work and those used in [6]:

$$w_\alpha = \omega_\alpha, \quad \mathbf{q}_h = \frac{5}{2}kT_h \mathbf{J}_a + \frac{5}{2}kT_h \mathbf{J}_i + \mathbf{h}_{hp}, \quad \mathbf{q}_e = \frac{5}{2}kT_e \mathbf{J}_e + \mathbf{h}_e,$$

$$(21)$$

$R^{(e)}_{ea} + R^{(e)}_{ei}$ is represented by the last term on the rhs of equation (11) of [6], $W^{(e)}_a = W^{(e)}_i = 0$, $W^{(e)}_e = -w^{(e)}_e$. Here the indices i, a, and e refer to ions, atoms, and electrons, respectively.

Appendix B. Transforming the equations for numerical solution

Given that the species conservation equations are linearly dependent, the equation of conservation of the atoms,

equation (13) with $\alpha = a$, is discarded. The species transport (Stefan–Maxwell) equations are linearly dependent as well; therefore, the Stefan–Maxwell equation for the atoms is also discarded. The atomic density is eliminated from the remaining equations by means of equation (1). The atomic transport velocity, which appears in the Stefan–Maxwell equations for the ions and the electrons, is eliminated by means of the relation $n_a V_a + n_i V_i = 0$, which follows from equation (12) after the electron contribution is dropped.

Solving the Stefan–Maxwell equations for the ions and the electrons (with V_a eliminated) for J_i and J_e and substituting the obtained expressions into the conservation equations for the ions and the electrons, one obtains parabolic equations for n_i and n_e, which are convenient for numerical solution.

An alternative approach, which allows direct implementation of the boundary condition (9), is as follows. The electron conservation equation, equation (13) for $\alpha = e$, is replaced with the current continuity equation, equation (16). In the 1D approximation, the latter equation assumes the form coinciding with that of the boundary condition (9). The electron number density is eliminated by means of the Gauss law. (Note that the Stefan–Maxwell equation for the electrons after this elimination involves the derivative $\partial^2 E / \partial x^2$, which resulted from the term $\partial p_e / \partial x$.) Solving equation (9) jointly with the Stefan–Maxwell equation for the ions, one obtains expressions for J_i and J_e in terms of $j - \varepsilon_0 \partial E / \partial t$, E, and spatial derivatives of n_i, T_h, and T_e. Substituting the obtained expression for J_i into the ion conservation equation, one obtains a parabolic equation for n_i. Substituting the expressions for J_i and J_e into the Stefan–Maxwell equation for the electrons, one obtains a parabolic equation for E. Note that this approach differs from the one used in [6] in two aspects: it is valid for the non-stationary case and the dependent variables are n_i and E (rather than n_e and E, as in [6]).

Appendix C. Analytical estimate of ion diffusion current

The aim of this appendix is to estimate the maximum current density that can be transported by the ambipolar diffusion of the ions from the bulk of atmospheric-pressure arcs to the surface of a non-emitting cathode.

If the arc current exceeds, say, 100 A, then the plasma in the arc bulk is in a state of local thermodynamic equilibrium, or LTE, meaning that thermal equilibrium holds, i.e. the electron and heavy-particle temperatures T_e and T_h are close, and ionization equilibrium holds, so the partial composition of the plasma may be found from equilibrium calculations neglecting particle transport.

The ionization equilibrium, while holding in the bulk of the plasma, is violated in a thin layer adjacent to the near-cathode space-charge sheath: the so-called ionization layer. If the ionization of neutral atoms occurs primarily in the quasi-neutral plasma, then the maximum ion current that can be extracted from the plasma (ion saturation current) is limited

by ambipolar diffusion of the ions across the ionization layer. Let us consider the simplest case, where the plasma is atomic. Ionization by electron impact is the dominant channel of ionization of neutral atoms in atomic thermal plasmas. If the ions are predominantly singly charged in the ionization layer and variations of the temperatures of the electrons and the heavy particles, T_e and T_h, may be neglected, then the maximum ion current (ion saturation current) from the ionization layer to an absorbing metal surface may be estimated with the use of an analytical solution of the ambipolar diffusion equation and written as [53]

$$j_i = e D_a \frac{n_i^{(S)}}{d}, \quad D_a = D_{ia}\left(1 + \frac{T_e}{T_h}\right), \quad d = \frac{1}{C_2}\sqrt{\frac{D_a k T_h}{k_i p}}. \tag{22}$$

Here, D_{ia} is the coefficient of binary diffusion of the ions and the atoms; $n_i^{(S)}$ is the charged particle density at the 'edge' of the ionization layer, which may be evaluated by means of the Saha equation in terms of T_e, T_h, and the plasma pressure p; C_2 is the numerical coefficient defined by equation (14) of [53], which depends on the ratio T_e/T_h and varies between approximately 0.67 and 1; and k_i is the rate constant of ionization of neutral atoms by electron impact, which includes both direct and stepwise ionization and is a function of T_e. Note that D_a has the meaning of the ambipolar diffusion coefficient, d is usually called the ionization length and represents a scale of thickness of the ionization layer.

As an example, the ion saturation current density computed by means of the first equation in equation (22) for the electron temperature value $T_e = 20\,000$ K and the heavy-particle temperature T_h varying over the range from the room temperature to T_e is depicted in figure 12; plasma-producing gas is argon or air and the plasma pressure is atmospheric. One can see that the ion saturation current density is of the order of 10^7 A m^{-2}.

Also shown in figure 12 are the ionization length d, the Debye length λ_D, and the mean free path for collisions between the ions and neutral atoms $\lambda_{ia} = \left[\left(n_a^{(S)} + n_i^{(S)}\right) \bar{Q}_{ia}^{(1,1)}\right]^{-1}$, where $n_a^{(S)}$ is the number density of the atoms at the edge of the ionization layer and $\bar{Q}_{ia}^{(1,1)}$ is the average cross section for momentum transfer in ion–atom collisions. Conditions of the validity of equation (22) read $\lambda_D, \lambda_{ia} \ll d$. One can see that the inequality $\lambda_D \ll d$ is satisfied. The inequality $\lambda_{ia} \ll d$ is satisfied for T_h values of the order of several thousand kelvin and higher but not for lower values of T_h, where the ion mean free path λ_{ia} and the ionization length d are comparable.

Hence, the ion motion across the ionization layer is not necessarily dominated by collisions in the conditions considered and equation (22), which is based on the diffusion treatment, is inaccurate. An approximate theory for conditions where λ_{ia} is comparable to d was developed by means of the so-called multifluid approach [54]. The ion current evaluated by means of [54, equation (50)] with the coefficient
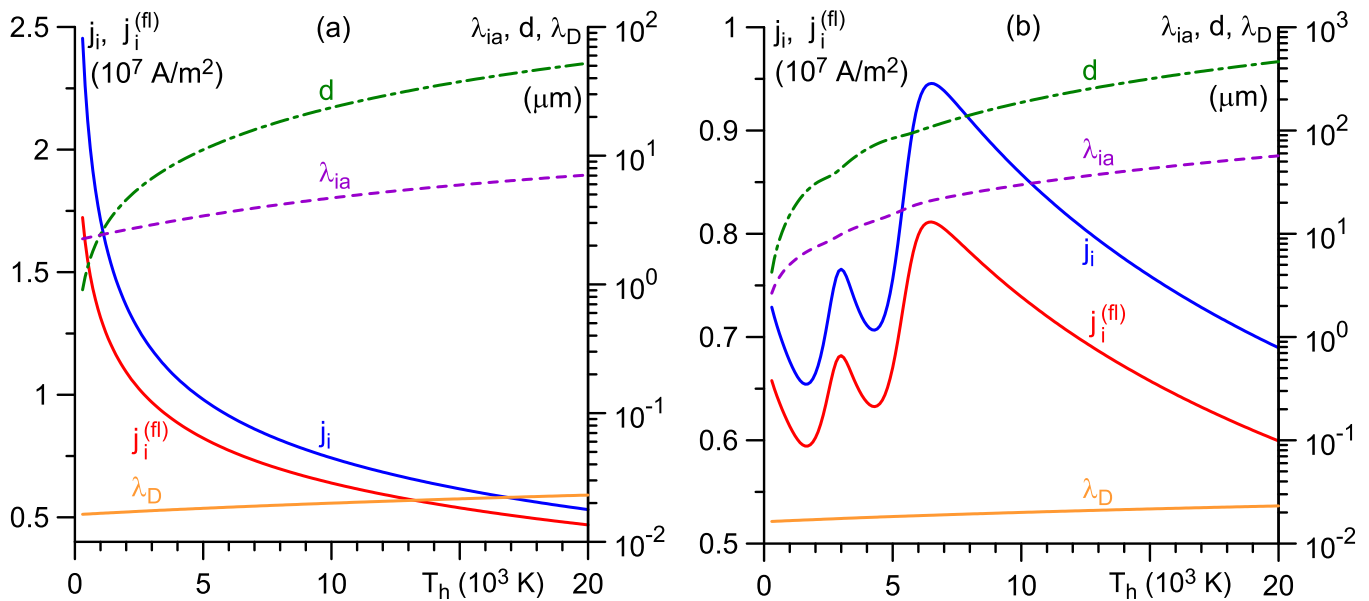
Figure 12. Ion saturation current density and characteristic length scales. Argon (a) and air (b) plasma, $p = 1$ bar, $T_e = 20\,000$ K.

C_1 replaced by C_2 given by [53, equation (14)] is depicted by the curve marked $j_i^{(fl)}$ in figure 12. One can see that $j_i^{(fl)}$ is not notably different from the diffusion value $j_i^{(d)}$ in these conditions.

ORCID iDs

D F N Santos ⓘ https://orcid.org/0000-0002-2377-766X
N A Almeida ⓘ https://orcid.org/0000-0002-6499-3609
M S Benilov ⓘ https://orcid.org/0000-0001-9059-1948

References

[1] Choquet I 2018 *Weld. World* **62** 177
[2] Benilov M S 2020 *J. Phys. D: Appl. Phys.* **53** 013002
[3] Murphy A B 2015 *Plasma Chem. Plasma Process.* **35** 471
[4] Boulos M I, Fauchais P and Pfender E 2016 *Handbook of Thermal Plasmas* (Berlin: Springer)
[5] Lowke J J, Murphy A B and Tanaka M 2019 *J. Phys. D: Appl. Phys.* **52** 444004
[6] Almeida N A, Benilov M S and Naidis G V 2008 *J. Phys. D: Appl. Phys.* **41** 245201
[7] Almeida N A, Benilov M S, Hechtfischer U and Naidis G V 2009 *J. Phys. D: Appl. Phys.* **42** 045210
[8] Kolev S and Bogaerts A 2015 *Plasma Sources Sci. Technol.* **24** 015025
[9] Semenov I L, Krivtsun I V and Reisgen U 2016 *J. Phys. D: Appl. Phys.* **49** 105204
[10] Saifutdinov A I, Fairushin I I and Kashapov N F 2016 *JETP Lett.* **104** 180
[11] Eliseev S I, Kudryavtsev A, Liu H, Ning Z, Yu D and Chirtsov A S 2016 *IEEE Trans. Plasma Sci.* **44** 2536
[12] Kolev S, Sun S, Trenchev G, Wang W, Wang H and Bogaerts A 2017 *Plasma Process. Polym.* **14** 1600110
[13] Khrabry A, Kaganovich I D, Nemchinsky V and Khodak A 2018 *Phys. Plasmas* **25** 013521
[14] Khrabry A, Kaganovich I D, Nemchinsky V and Khodak A 2018 *Phys. Plasmas* **25** 013522
[15] Baeva M, Loffhagen D, Becker M M and Uhrlandt D 2019 *Plasma Chem. Plasma Process.* **39** 949
[16] Baeva M, Loffhagen D and Uhrlandt D 2019 *Plasma Chem. Plasma Process.* **39** 1359
[17] Baeva M, Uhrlandt D and Loffhagen D 2020 *Japan. J. Appl. Phys.* **59** SHHC05
[18] Nandelstädt D, Redwitz M, Dabringhausen L, Luhmann J, Lichtenberg S and Mentel J 2002 *J. Phys. D: Appl. Phys.* **35** 1639
[19] Mitchner M and Kruger C H 1973 *Partially Ionized Gases* (New York: Wiley)
[20] Ferziger J H and Kaper H G 1972 *Mathematical Theory of Transport Processes in Gases* (Amsterdam: North-Holland)
[21] COMSOL Multiphysics® v. 5.4 2018 COMSOL AB (Available at: https://www.comsol.com/)
[22] Baeva M 2017 *Plasma Chem. Plasma Process.* **37** 341
[23] Almeida R M S, Benilov M S and Naidis G V 2000 *J. Phys. D: Appl. Phys.* **33** 960
[24] Phelps A V and Lj Z 1999 Petrović *Plasma Sources Sci. Technol.* **8** R21
[25] Raizer Y P 1991 *Gas Discharge Physics* (Berlin: Springer)
[26] Fomenko V S 1981 *Emission Properties of Materials* 4th edn (Keiv: Naukova Dumka) (in Russian)
[27] ELEM 2019 On-line tool for evaluation of the field to thermo-field to thermionic electron emission current density (available at: https://fisica.uma.pt/public-domain/simulation-tools/elem/)
[28] Murphy E L and Good R H 1956 *Phys. Rev.* **102** 1464
[29] Benilov M S and Benilova L G 2013 *J. Appl. Phys.* **114** 063307
[30] Polishchuk V P *et al* 2020 *High Temp.* **58** 476
[31] Sun S-R, Wang H-X and Zhu T 2020 *Contrib. Plasma Phys.* **60** e201900094
[32] Tolias P 2017 *Nucl. Mater. Energy* **13** 42
[33] Cunha M D, Kaufmann H T C, Benilov M S, Hartmann W and Wenzel N 2017 *IEEE Trans. Plasma Sci.* **45** 2060
[34] White G K and Minges M L 1997 *Int. J. Thermophys.* **18** 1269
[35] Touloukian Y S, Powell R W, Ho C Y and Clemens P G 1970 *Thermal Conductivity: Metallic Elements and Alloys* vol 1 (New York: Plenum)
[36] Loeb L B 1939 *Fundamental Processes of Electrical Discharge in Gases* (New York: Wiley)
[37] Latham R V and Xu N S 1991 *Vacuum* **42** 1173

[38] R V Latham (ed) 1995 *High Voltage Vacuum Insulation: Basic Concepts and Technological Practice* (New York: Academic)

[39] Wuensch W 2019 *8th Int. Workshop on Mechanisms of Vacuum Arcs* (*Padova, Italy, 15–19 September 2019*) p 85

[40] Paulini J, Klein T and Simon G 1993 *J. Phys. D: Appl. Phys.* **26** 1310

[41] Gayet R, Harel C, Josso T and Jouin H 1996 *J. Phys. D: Appl. Phys.* **29** 3063

[42] Baeva M 2018 *AIP Adv.* **8** 085322

[43] Benilov M S and Cunha M D 2003 *Phys. Rev.* E **68** 056407

[44] Mokrov O, Simon M, Sharma R and Reisgen U 2019 *J. Phys. D: Appl. Phys.* **52** 364003

[45] Mesyats G A and Uimanov I V 2015 *IEEE Trans. Plasma Sci.* **43** 2241

[46] Mesyats G A and Uimanov I V 2017 *IEEE Trans. Plasma Sci.* **45** 2087

[47] Kaufmann H T C, Cunha M D, Benilov M S, Hartmann W and Wenzel N 2017 *J. Appl. Phys.* **122** 163303

[48] Zhang X, Wang L, Jia S and Shmelev D L 2017 *J. Phys. D: Appl. Phys.* **50** 455203

[49] Wang L, Zhang X, Wang Y, Yang Z and Jia S 2018 *Phys. Plasmas* **25** 043511

[50] Zhang X, Wang L, Ma J, Wang Y and Jia S 2019 *J. Phys. D: Appl. Phys.* **52** 035204

[51] Kaufmann H T C, Silva C and Benilov M S 2019 *Plasma Phys. Control. Fusion* **61** 095001

[52] Hirschfelder J O, Curtiss C F and Bird R B 1964 *Molecular Theory of Gases and Liquids* (New York: Wiley)

[53] Benilov M S 1999 *J. Phys. D: Appl. Phys.* **32** 257

[54] Benilov M S and Naidis G V 1998 *Phys. Rev.* E **57** 2230